NORWAY

INTERN RAPPORT VM–60

AD-A062 800

INVESTIGATION OF UNDERGROUND EXPLOSIONS WITH MODEL TESTS: MEASUREMENTS IN THE TUBE

by

S Rollvik and M Vigstad

OCT 1978

FORSVARETS FORSKNINGSINSTITUTT
NORWEGIAN DEFENCE RESEARCH ESTABLISHMENT
P O Box 25 - N-2007 Kjeller, Norway

DISCLAIMER NOTICE

THIS DOCUMENT IS BEST QUALITY PRACTICABLE. THE COPY FURNISHED TO DDC CONTAINED A SIGNIFICANT NUMBER OF PAGES WHICH DO NOT REPRODUCE LEGIBLY.

FFIVM
Intern rapport VM-60
Reference: 261/130:738
Date: March 1978

INVESTIGATION OF UNDERGROUND EXPLOSIONS WITH MODEL TESTS: MEASUREMENTS IN THE TUBE

by

S Rollvik and M Vigstad

Godkjent
Kjeller 19 oktober 1978

T. Krog

T Krog
Forskningssjef

FORSVARETS FORSKNINGSINSTITUTT
Norwegian Defence Research Establishment
PO Box 25 - N-2007 Kjeller
Norway

CONTENTS

INVESTIGATION OF UNDERGROUND EXPLOSIONS WITH MODEL TESTS: MEASUREMENTS IN THE TUBE

SUMMARY

Model tests in three scales were undertaken to examine if simple scaling laws can be used to investigate underground explosions. Charges were detonated in steel tubes, and pressures and arrival times were measured in the tube and on a platform. This report describes the results from the measurements in the tube. A systematic deviation from the scaling laws is observed. The dependence of this deviation on tube diameter, charge weight and wall roughness is examined.

The results from the measurements on the platform are given in Ref (1). A detailed description of the experimental upset is given in Ref (2) and of the data processing in Ref (3).

1 INTRODUCTION

This report describes the results from tests performed to examine if simple scaling laws can be verified for the prediction of the blast wave following an accidental explosion in an underground ammunition storage site. Such scaling laws have been verified for explosions in free air, and it has been proposed that simple scaling laws also may be used in the underground case (4), (5), (6).

There are, however, many effects which obviously do not scale according to these laws. These effects may be of such a low order of magnitude that for practical purposes they are negligible. This has, however, not yet been sufficiently verified.

The objective of our tests was to compare the shock parameters, front pressure and front velocity, when TNT-charges of different weights were detonated in models in different scales, and to see if there was any deviation of importance from the scaling laws. Models of a simplified underground storage

site were therefore built in three scales. The models consist of a tube, simulating a tunnel, and a platform, simulating a flat terrain. The scales are 1:100, 2:100 and 3:100 of a natural size. TNT-charges were detonated and the pressure time history of the resulting blast was recorded at measurement stations in the tube and on the platform.

The results from the measurements inside the tube are described in the present report, while the results from the measurements on the platform are described in Ref (1). The experimental equipment is described in Ref (2) together with the methods for recording the data on analog tapes. The data are digitalized and are processed on a CYBER 74 computer. This is described in Ref (3).

Some of the results from the tests have been published in a preliminary report (4).

2 SCALING LAWS

In Figure 2.1 is shown a sketch of the tube with the charge. The tube has diameter D. The cylindrical charge has a diameter νD and length d. The charge weight Q is then proportional to dD^2. The pressure in the undisturbed air ahead of the shock front is P_1, and the pressure immediately behind the front is P_2. If only these parameters are used to describe the problem it follows from dimensionless analysis that the front overpressure

$$P = \frac{P_2 - P_1}{P_1} \qquad (2.1)$$

in a distance L from the charge center can be expressed as a function of the form

$$P = f\left(\frac{L}{d} , \frac{d}{D}\right) \tag{2.2}$$

If we introduce the charge weight Q in this equation, we obtain

$$P = f\left(\frac{LD^2}{Q} , \frac{Q}{D^3}\right) \tag{2.3}$$

It will be convenient to introduce a parameter q, called charge group, defined by the equation

$$q = \frac{Q}{D^3} \tag{2.4}$$

It is also convenient to introduce a dimensionless parameter for distance, namely

$$n = \frac{L}{D} \tag{2.5}$$

n measures the distance of the shock front from the charge center in number of tube diameters.

With n and q introduced the scaling law takes the form

$$P = f\left(\frac{n}{q} , q\right) \tag{2.6}$$

It states that for each tube diameter D the front pressure will be the same at the same position, when measured in number of tube diameters, and when the charges detonated belong to the same charge group, i e have the same value of q. We shall call this scaling with respect to dimension.

Since q is proportional to $\frac{d}{D}$ it describes the geometrical conditions in the vicinity of the charge. In a position not too close to the charge, it is a reasonable assumption that this term in the argument of f may be neglected, leaving the scaling law on the simple form

$$P = f(L_S) \tag{2.7}$$

where

$$L_S = \frac{n}{q} = \frac{LD^2}{Q} \tag{2.8}$$

is called scaled distance.

For the same tube diameter the front pressure will be the same for different charge groups when it is measured in the same scaled distance L_S, i e when $\frac{n}{q}$ is held fixed. This is called self similarity.

By similar arguments as above the arrival time t of the shock front in a position L is given by a functional relation of the form

$$t_s = g(L_S, q) \tag{2.9}$$

where we have introduced the scaled time

$$t_s = \frac{tD^2}{Q} = \frac{t}{qD} \tag{2.10}$$

At a sufficiently large distance from the charge, this scaling law is assumed to reduce to the simple relation

$$t_s = g(L_S) \tag{2.11}$$

The scaling laws (2.7) and (2.11) were proposed by Erikson (5) in 1964 for the propagation of blast in a tube.

The validity of these scaling laws will be examined in this report.

3 DESCRIPTION OF THE EXPERIMENTS

3.1 Description of the models

The models consist of two parts. One is the tube which simulates the underground tunnel. The other is the platform section consisting of a vertical steel plate above the tube outlet and a horizontal platform, simulating a steep mountain side and a flat terrain respectively.

The tubes are designed to provide two different model configurations.

The first configuration (CFG1) consists in principle of a straight tube with a detonation section in the middle as shown in figure 3.1.

The second configuration (CFG2) in principle consists of a straight tube connected to a detonation chamber in the one end. The other end leads to the platform as shown in figure 3.2. The cross section area of the detonation chamber is twice the cross section area of the tube.

The tunnel diameters in both configurations are 0.05 m, 0.10 m and 0.15 m respectively for the scales 1:100, 2:100 and 3:100.

Both models were made to allow for the mounting of pressure transducers along the tubes, one for each four diameter length. Pressure transducers were also mounted on the platform along the projection of the extended tube axis with one per each 0.5 m approximately. See figures 3.3 and 3.4.

Both configurations allow for a large-scale roughness in the tubes to take three different values, $r_L = 0$, $r_L = 0.03$ and $r_L = 0.06$. The large-scale roughness r_L is defined by the relation

$$r_L = \frac{\Delta D}{D} \qquad (3.1)$$

D is the tube diameter and $2\Delta D$ is the height of the roughness element as shown in figure 3.5.

The charges are pressed TNT charges. They are of cylindrical shape and for both configurations the diameters are the same fraction ν of the tube diameter D in the three scales. $\nu = 0.38$ for CFG1 and $\nu = 0.29$ for CFG2. There is, however, some difference in the mounting of the igniters, as is described in further detail in Ref (2).

The measurements and recordings of the data are automatic. This is further described in Ref (2) and (3).

3.2 Rankine-Hugoniot equation

We have measured the arrival time of the shock front and the front pressure at different measurement stations. From the arrival time measurements the shock front velocity U can be calculated. The shock velocity U and the front overpressure P are related to each other by the Rankine-Hugoniot equation

$$P = (1 + \mu^2) \left(\frac{U^2}{a_o^2} - 1 \right) \qquad (3.2)$$

a_o is the speed of sound in the undisturbed air ahead of the shock front and

$$\mu^2 = \frac{\gamma - 1}{\gamma + 1} \qquad (3.3)$$

where γ is the adiabatic constant. This relation applies to an ideal gas. The value, $\gamma = 1.4$ for air is used in our calculations.

By this formula then, the pressure and arrival time measurements represent a double set of data.

3.3 Experimental series

The main series of experiments consisted of approximately three shots in each of six charge groups in the three scales and for the three values of wall roughness and the two configurations. The charge groups and the corresponding charge weights in the three scales are listed in Table 3.1 together with the corresponding loading densities.

The shots with the largest charges in scale 3:100, CFG2, were for different reasons only performed in the case of $r_L = 0$.

It was of interest to perform some shots with charge groups corresponding to smaller loading densities. This was done in scale 3:100 with $r_L = 0$ for both configurations. The charge weights used are listed in Table 3.2. Three shots were fired for each of the charge weights in each configuration.

3.4 Short description of the propagation of the blast

The charges are placed coaxially with the tubes. When the charge is detonated a blast wave will propagate through the tube and onto the platform. The pressure-time history and the arrival time of the shock front are measured and recorded at every measurement station in the tube and on the platform.

Figure 3.6 shows as an example the front pressure in the 13 measurement stations in the tube for three equal shots in scale 1:100, CFG1. We notice the low pressure close to the charge. The shock front needs some time to build up. This is partially due to the fact that the energy is not instant-

aneously released and that the initial expansion of the shock is approximately spherical. First after a set of reflections from the walls a front is built up. The distance at which the front is established varies with charge weight. At the fourth measurement station, 16 diameters from the charge center, it is always fully established. We shall denote these first 16 diameters the build-up region and treat it separately.

From position n = 16, where the shock is established, the shock wave may be described as one-dimensional (5) (6). In this region we shall study the attenuation of the front pressure as it propagates through the tube.

We see from Figure 3.6 that the pressure does not decay smoothly with distance. This does not only result from uncertainties in the pressure measurements. It is also due to physical effects such as reflections from the tube walls and to rarefaction waves overtaking the shock front. As a result of this complicated system of reflections and rarefaction waves we get the relatively large scatter of the measurements from equal shots, as seen in the figure. This scatter is observed in all the measurements. We shall call the region between position n = 16 and the tube outlet for the attenuation region, since the attenuation of the shock is the dominating feature.

We shall not include the measurement station in the tube outlet in this region, that is n = 52 for CFG1 and n = 60 for CFG2. When the shock waves passes through the outlet, it changes from one-dimensional to three-dimensional. This region will be studied separately in Ref (1), where also the attenuation of the shock on the platform will be examined.

3.5 Systematic errors

It is not easy to estimate the magnitude of the uncertainties of the measurements, but it is reasonable to believe that it is in the order of 10% for the pressure measurements and 5% for the arrival time measurements. This is discussed in Ref (3).

Two systematic errors related to the measurements should be mentioned.

One is that two different methods have been used in recording the front pressures, and the other is the effect of the igniters. They will be shortly described.

3.5.1 Differences in recording of front pressures and arrival times between the scales

The pressure time history of the blast at each measurement station was recorded on analog tapes (2). For the experiments in scale 1:100 these were played out, and the values of the front pressure were found by direct measurements on the resulting diagrams. For the experiments in scales 2:100 and 3:100 the results were transmitted to a digital tape, and the front pressures were found by an automatic routine (3).

For a number of shots both methods were used, and it was found that the automatic method usually gave somewhat lower values for the front pressures. The difference was of magnitude 2 bar. As a consequence, the recorded front pressures in scale 1:100 will have a tendency to be a little too high, compared with the other two scales.

A similar comparison showed that the automatic method gave arrival times of the shock about 0.01 ms larger than the manual method. This results in too small arrival times in scale 1:100 compared with the two larger scales. This

difference will be of importance at the measurement stations relatively close to the charge.

3.5.2 TNT-equivalence of the electric igniters

We have used microsecond electric igniters P no 8 from Nitro Nobel AB, Sweden. They are not of standard type. For the smallest charges the TNT-equivalence of the igniters may be of importance. Some shots were therefore made to determine this.

The shots were fired in scale 1:100, with $r_L = 0$ and in CFG2. Front pressures and arrival times were recorded at the 13 measurement stations in the tube. From the arrival times the front pressures were calculated by the Rankine-Hugoniot equation. The front pressures determined from the arrival times were in good accordance with the measured front pressures.

The front pressures resulting from a charge consisting of 10 g TNT and one electric igniter were compared with the front pressures from a charge consisting of 10 electric igniters. In the same manner a charge consisting of 20 g TNT and one ingiter was compared with a charge consisting of 20 igniters. There were fired 2 shots with 10 g TNT, 3 shots with 10 igniters, 2 shots with 20 g TNT and 2 shots with 20 igniters. The results are listed in Table 3.3.

If P' denotes the pressures resulting from TNT-charges and P" the pressures from the igniters, it was found that $\frac{P"}{P'}$ was approximately constant at the different measurement stations in the tube. For the shots with 10 g TNT and 10 igniters it was found to be $\frac{P"}{P'} = 0.78$ for the measured pressures and $\frac{P"}{P'} = 0.79$ for the calculated pressures. For the shots with 20 g TNT and 20 igniters it was $\frac{P"}{P'} = 0.81$ for both the measured and the calculated pressures.

For the order of magnitude analysis in which we are interested we shall assume that the pressures measured are proportional to the charge weight. If x denotes the TNT-equivalence of the igniters we obtain

$$\frac{P''}{P'} = \frac{10\ x}{10\ g + x} \tag{3.4}$$

for the case of 10 g TNT and 10 igniters, and

$$\frac{P''}{P'} = \frac{20\ x}{20\ g + x} \tag{3.5}$$

for the case of 20 g TNT and 20 igniters. This gives

$$x = 1.15\ g \tag{3.6}$$

in the first case and

$$x = 1.07\ g \tag{3.7}$$

in the second case.

This shows that the effect of the igniters is of some importance for the 10 g charge and the 20 g charge. The 10 g charge is effectively an 11 g charge and the 20 g charge is effectively a 21 g charge, representing an increase of 10 and 5 percent, respectively. Therefore, when the results from these shots are compared to the shots with the same charge groups in the two larger scales, the pressures in scale 1:100 are somewhat too high.

This effect will be of no importance for larger charge groups.

3.6 Short review of the results

As mentioned, the main series of shots consisted of 3 shots for each combination of the different charge groups, scales, configurations and degrees of roughness. This gives a total of about 350 shots. For every shot the arrival time of the shock front of the blast and its pressure time history were recorded at each measurement station. The front pressure and maximum pressure were specially extracted from the pressure-time history. The work reported here is mainly based upon the study of front pressure, maximum pressure and time of arrival of the shock front at each of the 3 measurement stations in the build-up region and the 9 in the attenuation region. The conclusions presented in the following are thus based upon a total amount of data on about 350 * (3+9) * 3 = 12 600.

3.6.1 Deviation with respect to dimension

Let us as an example look at the results for one charge group, q = 160 kg/m^3. Figure 3.7 shows the mean values of the front pressure in the build-up and attenuation region for the three scales. According to the scaling law, eq (2.7) this should be three overlapping curves. At first sight these curves may seem to be equal when compared to the scatter of the pressures from equal shots, as shown in Figure 3.6. As a mean value, however, the pressure increases with increasing scale.

Figures 3.8, a-d, show the front pressure as a function of tube diameter for some charge groups and positions. According to the scaling law, these should be straight, horizontal lines. Although we can observe all kinds of curve forms, on the whole the pressure increases with increasing scale.

The question is, however, whether the increase is so strong compared to the data scatter that it must be concluded that the scaling law is not valid according to our data. To answer this, a systematic statistical examination is necessary, which will be presented in the next chapter.

3.6.2 Deviation from self-similarity

According to self-similarity one should for each scale measure the same front pressure when the scaled distance $L_s = \frac{n}{q}$ is fixed. Figures 3.9, a-c, show the front pressure as a function of charge group for some values of L_s in different scales. These should be straight, horizontal lines. Again, we observe all kinds of curve forms, but on the whole, the pressure decreases with increasing charge group. It thus seems that an increase in distance from the charge is not sufficiently compensated for by increasing the charge weight with the same factor.

Again, however, a systematic statistical analysis is necessary to decide if the deviation is a real one, or if it might be explained by the scatter of the measurements.

4 LINEAR REGRESSION

4.1 Deviation from scaling. Students T-test

The discussion in the preceeding chapter showed the necessity of a statistical analysis of the data. It will be presented here.

In chapter 2 we formulated the scaling laws

$$P = f(L_s) \qquad (2.7)$$

and

$$t_s = g(L_s) \qquad (2.11)$$

We shall examine the possibility of a deviation from these scaling laws, and we let the deviation be a linear expression in D, q and n. That is, we assume

$$P = f(L_s) + \alpha_1 D + \alpha_2 q + \alpha_3 n$$

$$= f(L_s) + \alpha_1 D + [\alpha_2 + \alpha_3 L_s] q \qquad (4.1)$$

and

$$t_s = g(L_s) + \alpha_1' D + \alpha_2' q + \alpha_3' n$$

$$= g(L_s) + \alpha_1' D + [\alpha_2' + \alpha_3' L_s] q \qquad (4.2)$$

where α_1, α_2, α_3 and α_1', α_2', α_3' are parameters to be determined by the data. α_1 and α_1' measure the deviation from Eqs (2.7) and (2.11) with respect to scale D. $[\alpha_2 - \alpha_3 L_s]$ and $[\alpha_2' + \alpha_3' L_s]$ measure the deviation from self-similarity.

The linear form does of course not necessarily represent the best fit to the deviation, but a possible non-zero deviation will be revealed. For the scaling laws not to be denied it is a necessary condition that the α-parameters turn out to be equal to zero. More precisely, they must be so close to zero that within the scatter of the data they can be said to be equal to zero. This is assessed by the Students T-test.

We shall test the following null-hypotheses:

H_o: $\alpha_1 = 0$ $\quad$ H_o: $\alpha_2 = 0$ $\quad$ H_o: $\alpha_3 = 0$

H_o: $\alpha_1' = 0$ $\quad$ H_o: $\alpha_2' = 0$ $\quad$ H_o: $\alpha_3' = 0$

The test level is ε, i e, the probability that the hypothesis is correct although we by the test-criterion has denied it, shall be less than ε. The test criterion is that H_o is denied if

$$T > C \qquad (4.3)$$

where T is Students T-statistic for the actual α-parameter, and C is the $\left(1 - \frac{\varepsilon}{2}\right)$-fractil for the Student distribution with N-2 degrees of freedom. N is the number of observations included in each test, which in this connection can be set equal to infinity.

The values of C for some values of test level ε are listed in Table 4.1.

In the next sections we shall give the results of these tests for the build-up region and the attenuation region.

4.2 Build-up region

The arguments used to establish that P and t_s are functions of n and q only through the scaled distance $L_s = \frac{n}{q}$, is valid in a region not too close to the charge. The self-similarity is in other words not supposed to be valid in the build-up region. Since there are only three measurement stations in this region, and because of the great scatter of the measurements, specially in position n = 4, the validity of self-similarity is not examined.

4.2.1 Deviation with scale

It is important to examine if there is established a deviation of the front pressure with scale already in the build-up region. In Table 4.2.a are shown the values of α_1 for the two configurations and the three degrees of wall roughness together with the corresponding values of T. $T > C$ in all cases for a test level $\varepsilon = 2\%$, and in four of the cases $T > C$ even for a level $\varepsilon = 0.2\%$. This shows that the hypothesis H_o: $\alpha_1 = 0$, must be denied.

α_1 is positive. This means that the front pressure increases with increasing scale. The variation within our three scales is about 10-20 bar, and since the magnitude of the pressures

in this region of the tube is about 100 bar, this deviation is appreciable.

The values of α_1' giving the deviation of the scaled arrival times with tube diameter are shown in Table 4.2b. The corresponding values of T are also shown. In CFG2 α_1' is negative, and H_o: $\alpha_1' = 0$ must be denied since $T > C$ on a test level $\varepsilon = 0.2\%$ in two cases and $\varepsilon = 1\%$ in one case. For CFG1 it seems that $\alpha_1' = 0$ is possible.

As described in section 3.5.1 the difference between the recording methods resulted in smaller values for the arrival time in scale 1:100 compared with the two larger scales. It seems likely that this fact explains why the tendency for the arrival times is not so clear as for the pressures.

Thus, it occurs to be a sound conclusion , when the results for the pressures and the arrival times are taken into account, that there is established a deviation from the scaling laws already in the build-up region. The front pressure, measured at the same scaled distance, increases with increasing scale.

4.3 Attenuation region

4.3.1 Deviation with scale

We shall first look at the deviation with tube diameter starting with the pressure measurements. The values of α_1 and T are shown in Table 4.3a. $T > C$ for both configurations and all values of r_L at the test level $\varepsilon = 0.2$. The hypothesis H_o: $\alpha_1 = 0$ must thus be denied. Since α_1 is positive in all cases, one must conclude that also in the attenuation region we will on the average observe higher pressures with increasing scale.

When we look at the arrival times, we find, just as we did for the build-up region, that the results are not quite clear.

Table 4.3b gives the values of α_1' and T. For CFG 1 with $r_L = 0$ α_1' is positive, while in the other cases it is negative In the three cases in CFG 2, H_o: $\alpha_1' = 0$ must be denied on a level $\varepsilon = 0.2\%$, while for CFG 1 with $r_L = 0.06$ it must be denied with $\varepsilon = 1\%$, and for $r_L = 0.03$ it must be denied with a test level $\varepsilon = 20\%$.

In summary, for the time measurements, H_o: $\alpha_1' = 0$ must be denied, and the arrival time is found in most cases to decrease with increasing scale, this being consistent with the observation that the front pressures increase with increasing scale.

One must conclude that also in the attenuation region the front pressures are larger in the larger scales. The method presented here does not reveal how the deviation in pressure with scale varies in the different positions in the tube. This will be studied in chapter 4 in connection with the curvefitting procedure.

4.3.2 Deviation from self-similarity

Table 4.4a gives the values of α_2 and α_3 together with the respective values of T. On a level $\varepsilon = 2\%$ the hypothesis, H_o: $\alpha_2 = 0$, must be denied in all the cases. The situation is not so clear for α_3, but when the values of T are compared with the values of C in table 3.1 it is reasonable also to deny the hypothesis H_o: $\alpha_3 = 0$. In every case $[\alpha_2 + \alpha_3 L_s]$ is different from zero. Since both α_2 and α_3 are negative, $[\alpha_2 + \alpha_3 L_s]$ is negative, and the deviation ΔP from self-similarity

$$\Delta P = q\,[\alpha_2 + \alpha_3 L_s] \qquad (4.4)$$

is negative. That is, the pressure decreases when the charge increases, although the scaled distance L_s is constant. We also notice that the deviation from selfsimilarity is larger for larger values of L_s.

The time measurements give similar results. The values of α_2' and α_3' together with the corresponding values of T are shown in table 4.4b. Except for one case, H_o: $\alpha_2' = 0$ and H_o: $\alpha_3' = 0$ must be denied. Although α_2' is negative, α_3' is positive and sufficiently large so that the deviation of scaled time from self-similarity,

$$\Delta t_s = q(\alpha_2' + \alpha_3' L_s) \qquad (4.5)$$

is positive and increasing with increasing charge weight, except for the smallest values of L_s. This positive deviation in scaled arrival time is equivalent to a negative deviation in front pressure.

4.4 Summary

It has been shown in this chapter that the scaling laws, eqs(2.7) and (2.11) neither in the build-up region nor in the attenuation region are confirmed by our measurements. The deviation is not so small that it can be explained by the scatter of the measurements.

It is desirable then, to describe the deviation in more detail, trying to explain the reasons for the deviation.

5 CURVE FITTING

5.1 Intrcduction

In chapter 2 we stated the scaling law

$$P = f(L_s) \qquad (2.8)$$

for the front pressure, preliminarily neglecting the functional form f.

It has been proposed to use (5)

$$P = f(L_s) = C_1 L_s^{-C_2} \qquad (5.1)$$

A curve-fitting procedure has now been used to determine values for the parameters C_1 and C_2 from the experimental data in the attenuation region. Since we have observed that the scaling law, eq (2.7) is not satisfied by our data, we must expect C_1 and C_2 to be functions of both scale and charge group. We also, of course, expect them to be dependent on wall roughness and configuration.

The curve fitting is performed by the method of least squares. This is done separately for shots belonging to the same configuration, wall roughness, scale and charge group. On the average then, the curve fitting is based on the measurements in the attenuation region for three equal shots, giving 27 corresponding values of pressure and position.

The results are listed in tables 5.1a - 5.1f. They show the values of C_1 and C_2 for each configuration, roughness, charge group and scale, together with the correlation coefficient, R.

We first notice the good correlation obtained, and that it is about equally good for each configuration, scale, roughness and charge group. For example, eq (5.1) does not seem to fit better to the tubes with $r_L = 0$ than to those with $r_L = 0.03$ or $r_L = 0.06$.

We notice that C_1 and C_2 are functions of q and D, and dependent on r_L and configuration, as they should be according to the analysis in chapter 4.

The curve fitting procedure will now be used to study the deviation from scaling more closely.

Since we have divided the tube into two regions, the build-up region and the attenuation region, it is convenient to express eq (5.1) in a slightly different form, namely

$$P = P_o \left(\frac{n}{16}\right)^{-C_2} \tag{5.2}$$

P_o is the front overpressure in position n = 16, that is at the beginning of the attenuation region. The pressure at this position is determined by what has happened in the build-up region. The relation between P_o and C_1, C_2 is

$$P_o = C_1 \left(\frac{q}{16}\right)^{C_2} \tag{5.3}$$

The values of P_o are also listed in the tables 5.1.

Since

$$C_2 = - \frac{d \ \ell n \ P}{d \ \ell n \ n} \tag{5.4}$$

it represents the attenuation of the front pressure in the attenuation region.

5.2 Behaviour of P_o

As mentioned in the last section P_o is the front overpressure at the beginning of the attenuation region in position n = 16. The values of P_o, obtained from the curve fitting based on pressure measurements from position n = 16 to the tube outlet, represent fairly well the measured values of front pressure at n = 16.

P_o is determined by the events in the build-up region. Since, however, the build-up region has been defined to be the 16 tube diameters closest to the charge, P_o is also to some

extent determined by the effects which are characteristic for the propagation of the shock front in the attenuation region. This is for example seen from the dependence of P_o on wall roughness. P_o decreases with increasing roughness.

We will more easily see how P_o qualitatively depends on q and D if we determine the parameters a and b so that a curve

$$P_o = aq^b \qquad (5.5)$$

is fitted to the experimental data.

The calculated values of a and b together with the correlation coefficient R are listed in table 5.2a for CFG 1 and table 5.2b for CFG 2.

We first notice the relatively good correlation for this curve form, indicating that it describes fairly well how P_o increases with increasing q.

It is seen that $b < 1$. This means that an increase in the charge group does not result in a proportional increase of P_o.

We also notice as a trend that a increases with increasing D, while b decreases with increasing D. This should mean that P_o is larger for the larger scales, but that the difference between the scales is smaller for the larger charge groups. The trends, however, are weak, and one should be careful in drawing conclusions.

5.3 Attenuation region

In this section the attenuation of the front pressure will be discussed, that is, the dependence of the attenuation on scale, charge group and roughness. Since C_2 represents the attenuation of the front pressure, we shall study how C_2 depends on these parameters.

We shall not make any quantitative statements, but concentrate on some qualitative features. We shall do this by fitting simple curve forms to the values found for C_2. That makes it easier to see qualitatively how C_2 depends on the different parameters. It should not be understood as an attempt to describe the real behaviour of C_2.

5.3.1 Dependence of C_2 on scale

We shall first look at the dependence of C_2 on tube diameter D. The values of C_2 and D are used to determine a linear curve

$$C_2 = a + bD \qquad (5.6)$$

and the results are listed in table 5.3a for CFG 1 and table 5.3b for CFG 2.

In CFG 1, $b < 0$ in all cases, except for one. This means that C_2 decreases when D increases, showing that the attenuation of the front pressure as the shock propagates through the tube is stronger for the smaller scales.

In table 5.4a a linear curve in charge group q is fitted to the values of b. The tendency is that b decreases when q increases. Since b measures the difference in attenuation between the three scales, it means that this difference becomes larger for larger charge groups.

For CFG 2, $b < 0$ in 8 cases and $b > 0$ in 7 cases. That is, no tendency of the attenuation to decrease with increasing scale is seen. This difference between CFG 1 and CFG 2 might be explained statistically, but it may also result from the different physical situations in the two configurations, as will be discussed in section 5.7.

From table 5.4b, where a linear curve in q is fitted to b, we see that for sufficiently large charge groups, b should become negative, as in CFG 1.

5.3.2 Dependence of C_2 on charge group

The curve

$$C_2 = a\, q^b \qquad (5.7)$$

is fitted to the values of C_2. The results are listed in table 5.5a for CFG 1 and table 5.5b for CFG 2. In both configurations b is negative, so that C_2 decreases when q increases. It means that the attenuation is smaller for the larger charge groups.

We also notice a weak tendency of b to decrease with increasing D. If that is true, it should mean that the effect of smaller attenuation for larger charge groups, is increasing with increasing scale. This is consistent with what was mentioned in the previous section.

It is a trend that b increases with increasing value of r_L, which would mean that the presence of large scale wall roughness tends to oppose the decreasing effect of increasing charge group on the attenuation. In other words, the damping of the front pressure when large scale wall roughness is present, is not so much decreased by increasing charge group, as it otherwise would.

5.3.3 Dependence of C_2 on large-scale wall roughness

As expected C_2 increases with increasing value of r_L. The attenuation of the front pressure is larger with larger roughness present.

In tables 5.6a for CFG 1 and table 5.6b for CFG 2, the linear form

$$C_2 = a + b\, r_L \qquad (5.8)$$

is fitted to the values of C_2.

b is positive, so that C_2 increases with increasing r_L. b decreases weakly with increasing scale. The increase in the attenuation with increasing r_L is, in other words, a little stronger for the smaller scales. The damping effect of a large wall roughness is thus somewhat stronger for the smaller scales than the larger ones.

With the presence of a large scale roughness $r_L > 0$, a deviation from scaling with respect to dimension is introduced.

One should, however, be a little careful in drawing conclusions. The decrease in b with scale is weak, and occurs in neither of the configurations between all the three scales for all charge groups.

5.3.4 Summary of the curve fitting procedure

The discussion in the preceeding sections can be summarized by fitting the linear expression

$$C_2 = \beta_1 + \beta_2 D + \beta_3 r_L + \beta_4 \ln q + \beta_5 D r_L + \beta_6 D \ln q + \beta_7 r_L \ln q \qquad (5.9)$$

to the values of C_2 for both configurations. Notice that the dependence of C_2 on charge group q in this expression is through ln q.

The resulting values of β and the partial correlations are listed in table 5.7. Some of the partial correlation coefficients are not significant. The scatter of the values of C_2 is too large to expect a good correlation to eq (5.9). However, eq (5.9) is not expected to give a quantitative description of the dependence of C_2 on q, r_L and D, but only to reveal some of the qualitative features of this dependence. To decide if the dependence of C_2 on each of the terms in eq (5.9) is significant, one should not only look at the partial correlation coefficients in table 5.7, but also at

the curve fitting procedures in the preceeding sections.

With the values of β_i inserted in eq (5.10), it takes the form

$$C_2 = 1.09 + 2.0\ D + 27.6\ r_L - 0.094\ \ell n\ q - 20\ D\ r_L - 0.55\ D\ \ell n\ q - 2.2\ r_L\ \ell n\ q \qquad (5.11a)$$

for CFG 1 and

$$C_2 = 1.47 + 2.75\ D - 6.16\ r_L - 0.175\ \ell n\ q - 24\ D\ r_L - 0.42\ D\ \ell n\ q + 2.7\ r_L\ \ell n\ q \qquad (5.11b)$$

for CFG 2.

We notice that $\frac{\partial^2 C_2}{\partial D\ \partial r_L}$ and $\frac{\partial^2 C_2}{\partial D\ \partial\ \ell n\ q}$

are negative in both configurations, indicating that the increase in C_2 with increasing scale is larger for larger charge groups and larger values of wall roughness.

$\frac{\partial^2 C_2}{\partial\ r_L\ \partial\ \ell n\ q}$ has different sign in the two configuration.

5.4 Comparisison with exponential curve form

In this chapter the front pressures in the attenuation region have been fitted to the curve form eq (5.1). It has been proposed that the decay in front pressure follows an exponential law (7), that is, that the front pressure in position n can be expressed as

$$P = P_o\ e^{-C_2(n-16)} \qquad (5.12)$$

where P_o is the front pressure in position n = 16.

We have not used this function for curve fitting to all our data, only for the case of $r_L = 0$ in CFG 1 we have made a comparison between the two curve forms. The comparison is made for each charge group and scale separately. The method used is one described by T J Dylewski in ref (8).

The curve forms are fitted to the data and the square deviation S is calculated for both curves. Then all the pressures in positions n = 16 to n = 32 are fitted to both curve forms and the square deviation S' is calculated for both. In a similar manner the square deviation S" for the fitting of the pressures in positions n = 36 to n = 48 is calculated for both. The curve form giving the smallest value of $\frac{S}{S' + S"}$ is the best one.

This has been done for each charge group and scale for CFG 1, $r_L = 0$, and the values are listed in table 5.8. The test gives different results for the different scales and charge groups, with each curve form preferred about the equal numbers of times.

5.5 Shots with small charges

The front pressures measured in the shots with the small charges in scale 3:100 were also used to determine C_1 and C_2 in eq (5.1). The resulting values of C_1, C_2, P_o and the correlation coefficient R are listed in tables 5.9a and 5.9b for CFG 1 and CFG 2 respectively. We notice the good correlation obtained also in this case.

5.5.1 Build-up region

The values of P_o are fitted to eq (5.5) giving

$$P_o = 4.0\ q^{0.64}$$

with a correlation R = 1.00 for CFG 1, and

$$P_o = 5.5\ q^{0.54}$$

with R = 0.93 for CFG 2. When this is compared with the corresponding results for the larger charges in the main experimental series (see tables 5.2a & b),

$$P_o = 36.8\ q^{0.15}$$

for CFG 1 and

$$P_o = 28.2\ q^{0.20}$$

for CFG 2, it is seen that P_o increases faster with charge for the smaller charges than for the larger. The increase in P_o is not proportional to the increase in q, however.

P_o as a function of q is shown in figure 5.1a for CFG 1 and in figure 5.1b for CFG 2. The figures indicate that there is a limit on the pressures which can be obtained by increasing the charge weight.

5.5.2 Attenuation region

A linear expression in ℓn q is fitted to the values of C_2, resulting in

$$C_2 = 1.56 - 0.198\ \ell n\ q$$

with correlation R = 0.97 for CFG 1 and

$$C_2 = 0.88 - 0.009\ \ell n\ q$$

with the poor correlation R = 0.14 for CFG 2

When this is compared with the corresponding results for the main series (eq 5.11).

$$C_2 = 1.39 - 0.177\ \ell n\ q$$

for CFG 1 and

$$C_2 = 1.88 - 0.238 \ln q$$

for CFG 2, it is seen that the decrease in C_2 with increasing charge is about the same or somewhat larger for the larger charges than the smaller ones.

C_2 is shown as a function of q in figure 5.2a for CFG 1 and figure 5.2b for CFG 2.

5.6 Comparison with NDCS

The results in this chapter will now be compared with results obtained at the Norwegian Defence Construction Service (NDCS) (6). Two of the tubes described in ref (6) were of steel. They were open in both ends, and the charges were detonated in the middle of the tubes. The tube diameters were D = 0.05 m and D = 0.20 m, corresponding to scales 1:100 and 4:100, respectively. The large scale roughness, as defined in this report, was $r_L = 0$. In the tube with D = 0.05 m the charges used ranged from 9.5 g to 17.5 g, corresponding to charge groups q = 76 kg/m^3 and 140 kg/m^3. In the tube with D = 0.20 m, the charge weights were in the range 9.5 g to 200 g, corresponding to charge groups q = 1.1875 kg/m^3 to 25 kg/m^3.

Eq (5.1) was fitted to the front pressures, resulting in

$$C_1 = 18$$

and

$$C_2 = 0.66$$

These values are in good accordance with our results. $C_2 = 0.66$ is larger than the values of C_2 in our main series of shots, but are in the range of values of C_2 in the shots

with small charges. The q-values in our shots with small charges are included in the range of q-values in the NDCS experiments. Also $C_1 = 18$ is smaller than the mean of the C_1-values in our main series, and is closer to the C_1-values obtained from the shots with small charges.

5.7 Difference between CFG 1 and CFG 2

In CFG 1 the tube end closest to the charge is open while in CFG 2 it is closed. This gives rise to important differences in the blast.

In CFG 1 a rarefaction wave will be reflected from the open end and propagate in the heated gas behind the shock front with a larger speed in the same direction. Sooner or later it will overtake the shock and attenuate it. The same will happen in CFG 2, but the wave reflected from the closed end will be a shock wave, thus increasing the front pressure of the first shock when it sooner or later catches it up.

As a rule of thumb the front pressure in CFG 2 should be the same as the front pressure in CFG 1 resulting from a charge twice as large.

What we observe, however, is smaller front pressures in CFG 2 than in CFG 1 in the tube. This must result from the other difference between the two configurations. In CFG 1 the charges are detonated in the tube, while in CFG 2 they are detonated in a detonation chamber with a cross-sectional area twice as large that of the tube. When the energy from a detonation in CFG 2 propagates from the chamber into the tube, it must be delayed by the decrease in cross-sectional area.

One difference between CFG 1 and CFG 2 can be seen from the curve fitting in section 5.2. Tables 5.2a & b give the values of a and b in the equation,

$$P_o = a\, q^b \qquad (5.5)$$

It is seen that b is larger for CFG 2 than for CFG 1, and that a is smaller for CFG 2 than for CFG 1. Thus, as seen from Tables 5.2, the values of P_o for q = 80 kg/m^3 are larger for CFG 1 than for CFG 2, but the increase with increasing q is greater in CFG 2.

We have not studied systematically the difference in pressure time histories of the blast in the two configurations, but a short examiation seems to indicate a difference as shown in figure 5.3. The blast has a larger front pressure, but a shorter positive duration in CFG 1 than in CFG 2. In CFG 2 a second peak is following the first peak some distance behind without overtaking it during the propagation through the tube.

6 DISCUSSION

6.1 Build-up region

In section 5.2 it was seen that P_o, the front pressure in position n = 16 at the beginning of the attenuation region, is an increasing function of charge group, but that the increase was smaller than a proportional increase. It was also seen that P_o increases with increasing scale, but that this increase is smaller for the larger charge groups. To that extent P_o obtained from the curve fitting really is determined by the build-up phase of the shock, it seems to indicate that there is an upper limit on the front pressures which can be obtained by increasing the loading density. This would be in accordance with a discussion by D R Curran in ref (9). He states that a wide range of initial pressure in the detonation chamber will produce initial air shock pressures which lie close together in a region about 100 bars.

We shall not go further into this problem. It would have been of interest, however, to study not only the front pressure, but the whole pressure-time history of the blast at the measurement stations closest to the charge.

Since it seems to be an upper limit on the initial front pressures, it must also be an upper limit on the deviation from scaling with respect to dimension. That is, the initial front pressure can not be very much larger in a full scale test than in a small scale test. So for the problem of extrapolating from model tests to full scale tests it seems to be more important to concentrate on the attenuation of the front pressure of the shock than its initial formation.

6.2 Attenuation region

There are two main sources for the attenuation of the front pressure as the shock propagates through the tube (6), (i) rarefaction waves which gradually overtake and eat up the shock front, (ii) wall roughness.

We defined a large-scale wall roughness r_L in section 3.1, eq (3.1) and our tubes provide three degrees of large scale roughness, $r_L = 0$, $r_L = 0.03$ and $r_L = 0.06$. This roughness leads to a complicated reflection and diffraction pattern of the shocks (10), giving rise to an attenuation of the front pressure.

There is an additional roughness which we shall call the small scale roughness, r_S. The walls in the tubes are not quite smooth. Both with $r_L = 0$, $r_L = 0.03$ and $r_L = 0.06$ there are irregularities of the size of grains of sand in the steel walls. We have measured the mean height, k, of these irregularities. For all the tubes in scale 1:100 it was found to be

$$k = 0.044 \text{ mm} \qquad (6.1a)$$

and for all the tubes in scales 2:100 and 3:100 it was

$$k = 0.080 \text{ mm} \tag{6.1b}$$

We shall define the small-scale roughness r_S by the relation

$$r_S = \frac{k}{D} \tag{6.2}$$

This gives

$$r_S = \begin{cases} 0.88 \cdot 10^{-3} & \text{for 1:100} \\ 0.80 \cdot 10^{-3} & \text{for 2:100} \\ 0.53 \cdot 10^{-3} & \text{for 3:100} \end{cases} \tag{6.3}$$

The total pressure loss can be expressed by the relation

$$\frac{dP}{dn} = \left(\frac{dP}{dn}\right)_R + \left(\frac{dP}{dn}\right)_{r_L} + \left(\frac{dP}{dn}\right)_{r_S} \tag{6.4}$$

where $\left(\frac{dP}{dn}\right)_R$ is the pressure loss due to overtaking rarefaction waves, and $\left(\frac{dP}{dn}\right)_{r_L}$ and $\left(\frac{dP}{dn}\right)_{r_S}$ are the pressure losses due to large-scale and small-scale roughness, respectively.

An understanding of each of these damping effects and of their relative importance would give an understanding of the total pressure attenuation, and then also of the dependence of the attenuation on scale.

6.3 Pressure loss due to rarefaction waves

Many models have been proposed for the shockfront attenuation due to overtaking rarefaction waves. One of them, proposed by Porzel (11) states that

$$\left(\frac{dp}{dn}\right)_R = f(P) \, \frac{1}{U} \, \frac{\partial P}{\partial t} \tag{6.5}$$

U is the shock velocity, $\frac{\partial P}{\partial t}$ is the slope of the rarefaction wave and f(P) is a function of the front overpressure.

In an air driven shock tube, where $\frac{\partial P}{\partial t} = 0$, there is no pressure loss due to rarefaction waves. For a peaked blast profile, $\frac{\partial P}{\partial t}$ is large, and the pressure loss will be large.

We have not examined the pressure-time profiles from our experiments, and consequently we can not determine the relative importance of the pressure loss due to rarefaction waves. Also, a detailed study of the difference in pressure-time profiles between CFG 1 and CFG 2 would give information about the rarefaction waves, since the tube end close to the charge is open in CFG 1 and closed in CFG 2.

6.4 Pressure loss due to large-scale roughness

We found in section 5.3.3 that the increase in C_2 with increasing r_L is larger for the smaller scales, which means that the damping effect of a non zero r_L is larger in the smaller scales. A scale dependence of the front pressure therefore results from the presence of a large-scale roughness.

The value of C_2 is high also in the case of $r_L = 0$, indicating that the large scale roughness can not be the only important source of the attenuation. A scale dependence of C_2 is also present for $r_L = 0$, so there must be additional effects which do not scale.

6.5 Pressure loss due to small-scale roughness

From eq (6.3) it was seen that the small scale roughness r_S in our experiments does not scale, i e, it has not the same values in all the three scales. To the extent the pressure loss due to this roughness is important for the total pressure

loss, it will lead to a dependence of the attenuation on scale.

The values of C_2 are relative large even in the case of $r_L = 0$, indicating that if the assumption in eq (6.4) is valid, an important part of the attenuation must be due to the small scale roughness and/or rarefaction waves. Also, since C_2 is scale dependent even when $r_L = 0$, there must be a scale dependence in at least one of these effects. Since we have not studied the effect of the rarefaction waves, we can not decide if this gives rise to a scale dependence or not. Because of the difference between CFG 1 with the open tube end and CFG 2 with the closed end with respect to rarefaction waves, one should perhaps expect a larger difference in the values of C_2 in the two configurations than we have observed, if overtaking rarefaction waves should be the main reason for the front pressure attenuation when $r_L = 0$.

Several experimental and theoretical investigations of the front pressure attenuation in air driven shock tubes indicate that a small scale roughness can result in an appreciable front pressure attenuation as a shock propagates through the tube (12), (13), (14), (15). The magnitude of the attenuation over a distance 50 to 100 tube diameters may be in the range of 20 to 80 percent.

We shall study the possibility that the main part of the deviation from scaling with respect to dimension when $r_L = 0$ might be explained by the pressure loss due to small-scale roughness.

6.6 The physical reason for the pressure loss due to small-scale roughness

The pressure loss due to the small-scale roughness may be explained in the same way as for the large scale roughness, namely that the projections give rise to a set of reflections

and diffractions of the shock which attenuates the front pressure (10). It may also, however, result from the viscous friction with the tube walls, arising in a turbulent boundary layer behind the shock.

It is difficult to decide which of these explanations is the most important one without a quantitative and more detailed study of the attenuation observed in our experiments. We shall in the following present a possible formulation of the problem if the pressure loss is caused by viscous friction.

6.7 Pressure loss due to viscous friction

The pressure loss dP due to viscous friction over a tube section of length dn is assumed to be independent of position n and proportional to the pressure at this position, i e:

$$\frac{dP}{dn} = KP \qquad (6.6)$$

where K is a constant.

By the Rankine-Hugoniot equations, this can also be expressed as

$$\frac{dP}{dn} = K(1 + \mu^2)(M_S^2 - 1) \qquad (6.7)$$

where M_S is the Mack number of the shock front, or, for strong shocks, approximately as

$$\frac{dP}{dn} = K \frac{(1 + \mu^2)}{(1 - \mu^2)^2} M_f^2 \qquad (6.8)$$

where M_f is the Mach number of the flow behind the shock.

Eq (6.6) was proposed by Emrich and Curtiss (16) after experiments with air driven shock tubes of different size and shape. Their tubes had zero large-scale roughness, and no rarefaction waves were present. They found K to be almost independent of n and only slowly varying with P. The value of K is about $3.5 \cdot 10^{-4}$. Their experiments comprised, however, only shock strengths up to $M_S = 3$.

One must expect $\frac{dP}{dn}$ to depend on the whole pressure-time history of the blast when passing position n. Specially, it must depend on the positive duration t_+ of the blast. At BRL K was proposed to be of the form (9)

$$K = K'(\alpha' + \frac{D}{t_+}) \tag{6.9}$$

with K' and α' approximately constant.

Eq (6.8) is of the same form as the standard formula for the pressure loss in a subsonic flow in a tube,

$$\frac{dP}{dn} = \lambda(\tfrac{1}{2}\ \rho\ w^2) \tag{6.10}$$

where w is the flow velocity and ρ the fluid density. λ is a factor which depends on the small scale roughness and the Reynolds number. For large Reynolds numbers λ becomes independent of Reynolds numbers, and can be expressed by the Nikuradse formula

$$\lambda = \frac{0.25}{(\lg \frac{3,715}{r_S})^2} \tag{6.11}$$

lg denotes the logarithm with base 10.
We shall assume that the small-scale roughness enters into eq (6.6) for a blast wave through the same factor as in eq (6.10) for a subsonic flow, and since the Reynolds numbers in our case are sufficiently large, the Nikuradse formula eq (6.11) will be used.

We shall in other words assume that K in eqs (6.6 - 6.8) is of the form

$$K = \alpha \cdot \frac{0.25}{\{\lg\ (\frac{3.75}{r_S})\}^2} = \alpha\lambda \qquad (6.12)$$

where α according to eq (6.9) depends on the positive duration t_+ of the blast.

6.8 Magnitude of pressure loss due to viscous friction

If we knew the formulae describing the pressure losses in eq(6.4) this equation could be integrated to give the front pressure as a function of position in the tube for the various tube dimensions, charge weights and values of large-scale roughness. However, this study will be restricted to a suggested relation for the pressure loss due to small-scale roughness when it is assumed to result from viscous friction to the walls.

We shall examine if this deviation due to small-scale roughness can be responsible for the total deviation from scaling in the attenuation of the front pressure. That is, we must examine if there is a value of α in eq (6.12) which is sufficiently large to be responsible for all the deviation observed and sufficiently small to avoid an unrealistic large pressure loss due to the small-scale roughness. We shall do this by trying to determine the values P' which the front pressure would have had at different positions in the tube for the three scales, if there had been no pressure loss due to small scale roughness. If all the deviation should be explained by this effect, the attenuation of P' should be the same for all scales.

Since this is more an illustration than a systematic analysis, we shall do it only for $r_L = 0$ in CFG 1.

The pressure loss ΔP over a tube length of 4 tube diameters between two succeeding measurement stations in positions, n-4 and n are calculated according to eqs (6.7) and (6.12).

$$\Delta P = 4 \cdot \frac{7}{6} \cdot \alpha\lambda (M_S^2 - 1) \qquad (6.13)$$

The value of the shock velocity U is set equal to $\frac{8D}{\Delta t}$ where Δt is the difference in arrival times between the positions n+4 and n-4. The value of U obtained in this way is associated with position n. Values of U are shown in table 6.1 for $r_L = 0$, CFG 1.

P' is obtained at a measurement station in position n by adding to the measured pressure P the sum of all the pressure losses between previous measurement stations. Because of the great scatter of P, we shall use the values $P = C_1 \left(\frac{q}{n}\right)^{C_2}$ from the curve fitting in chapter 5.

The arguments presented are of a somewhat approximate character, and a value of α can not be determined exactly. It is determined by the condition that the attenuation of P' should be independent of scale. If the attenuation is independent of scale, then the values of $\frac{P'(3:100)}{P'(2:100)}$ and $\frac{P'(2:100)}{P'(1:100)}$ are invariant with regard to n, and they are equal to $\frac{P_o(3:100)}{P_o(2:100)}$ and $\frac{P_o(2:100)}{P_o(1:100)}$ respectively, where P_o denotes an initial pressure. This turns out to be approximately satisfied for $\alpha = 0.6$ as is seen in table 6.2.

Figure 6.1 shows an example of P' as function of n together with the values of P obtained from the curve fitting for the three scales.

In position n = 48 the pressure loss due to eqs (6.6) and (6.12) with $\alpha = 0.6$ is about 60% of the total pressure loss. It then follows that if the pressure loss from the small scale roughness can be responsible for about 60% of the total pressure loss as the shock propagates through the tube, it can also be responsible for the deviation from scaling observed in the attenuation of the front.

60% is a very likely value for the small scale roughness pressure loss. Based on experiments at BRL a value between 20% and 80% has been proposed (13). Bobin and Thery (12) have done an examination of the pressure attenuation with help of a computational program. Although the pressures they have examined are much smaller than ours, and the tubes are much longer, their results should indicate a value of about 50%.

As a conclusion, it seems to be a possible hypothesis that the scale dependence in front pressure attenuation when $r_L = 0$, may result from viscous friction due to small-scale roughness.

It is emphasized, however, that to prove this hypothesis it is necessary to study the experimental data in much further detail.

6.9 Summary

Small-scale roughness, large-scale roughness and rarefaction waves are supposed to be the main reasons for the attenuation of the front pressure. The data have not been sufficiently analysed to give any quantitative statements of the relative importance of each of these effects. It is reasonable to assume that the deviation from scaling with respect to dimension is mainly due to the small scale roughness. It is not understood if the small-scale roughness pressure loss results primarily from viscous friction or from the diffraction pattern of the shock from the small wall-irregularities. Our data have not been analysed in such a way that we can decide which of these are most important. If the damping is assumed to result mainly from viscous friction, it is sufficient that this damping is about 60% of the total damping at the end of the tube, to associate all the scale dependence of the attenuation with the damping from small-scale roughness r_s.

7 EXTRAPOLATION TO FULL SCALE

7.1 Effect of small-scale roughness

If the assumptions in chapter 6 are valid, the front pressures in a full scale steel tube with D = 5 m and small scale roughness r_s can easily be found by using the values of P' obtained from model tests and subtracting the pressure loss due to small scale roughness as given by eq (6.6).

An example of full scale pressures obtained this way in steel tube with k = 0.080 mm ($r_s = 1.6 \cdot 10^{-5}$) is shown as the full drawn line in figure 6.1. Thismeans that if the assumptions in chapter 6 are valid the shock parameters in a full scale steel tube can be predicted by experiments in small scale steel tubes.

Figure 7.1 shows as an example how the front pressure in position n = 48 at the end of the attenuation region depends on scale, according to the formulae in chapter 6. k = 0.080 mm is used.

7.2 Real ammunition storage site

Real undergound ammunition storage sites are not made of steel, but are excavated in rock. For predicting shock parameters in this case from the shock parameters in the full scale steel case it is necessary with a knowledge of the different influence of steel and rock on the blast. Such an analysis will not be attempted here.

It is also necessary to determine the mechanism which causes the attenuation of the front pressure due to the actual roughness in the tunnel walls. The front pressures obtained in a full scale steel tube must, however, be assumed to represent an upper bound for the pressures which can be obtained in a geometrically similar tube in rock.

The geometrical conditions in an actual storage site are not as simple as in our models. We have not examined the effects on the blast resulting from more complex configurations. Effects not encountered in our simple models may enter into the problem under more complicated geometrical conditions.

7.3 Full scale tests

It would be of great importance to compare data from model- and full scale experimental series from several institutions to single out how different effects scale. We have not done such an examination of all existing experimental information. We have only studied the results from some full scale tests performed in Norway, and compared them with the present model tests. There are very many differences between the models and these full scale tests, so there are severe limitations on the conclusions which can be drawn.

A short review of the full scale model tests will be given in the rest of this chapter.

7.3.1 Tests at Raufoss

The Raufoss experiments are described in ref (17). The tunnel was closed in one end, and the diameter was 2.65 m, corresponding to scale 53:100. In some shots the charges were detonated in a sidechamber, while in four shots the charges were detonated in the tunnel. We shall look at the results from this last case. They must be compared with the results from shots with charges twice as large as in our CFG 1. In two shots the charge weight was 1000 kg, the only difference being that the charge in one case was closer to the tunnel end than in the other. The charge weights in the two other shots were 300 kg and 100 kg. This corresponds to charge groups 53.7 kg/m^3, 16.1 kg/m^3 and 5.37 kg/m^3. 5.37 kg/m^3 is much lower than we have had while the other two are in the range of values of our shots. The pressures

obtained in the Raufoss experiments are listed in table 7.1 together with some actual pressure measurements from our model tests. In the shots with small charges only tubes with $r_L = 0$ were used.

We see that the Raufoss pressures are very low. This may be due to the tunnel roughness and to the fact that the tunnel walls are of rock and not of steel. It may also be due to the considerable geometrical differences.

We have fitted eq (5.1) to the Raufoss pressures to see how the attenuation of the front pressure, represented by C_2, in this full scale case deviates from the attenuation in the model tests.

In section 5.3 the values of C_2 from CFG 1 in the main series of the model tests were represented by the equation

$$C_2 = 1.09 + 2.0\ D + 27.6\ r_L - 0.094\ \ln q - 20\ D\ r_L - 0.55\ D\ \ln q - 2.2\ r_L\ \ln q \qquad (5.11a)$$

If we insert in this equation $r_L = 0.06$, which should be the most probable value of the wall roughness in the Raufoss tunnel, and for q two times the actual q-values in the Raufoss shots, we can compare the attenuation found in the Raufoss shots with the attenuation found in the model tests. The results are shown in table 7.2. They seem to support the conclusion based on the model tests, that the attenuation of the front pressure decreaces with increasing scale. For the two Raufoss shots with $q = 53.7\ kg/m^3$ the values of C_2 are about as large or somewhat larger than the corresponding values of C_2 from the model tests. This may, however, be due to the different attenuating effect of rock and steel.

7.3.2 Tests at Lista

The Lista experiments are described in ref (9). The tunnel was open in both ends and had a square cross section. The area of the cross section was about 12 m^2, which corresponds to a hydraulic diameter D = 4 m or scale 80:100. The charges were detonated in the tunnel, so it corresponds to our CFG 1. The shots were fired with four charge weights, 10 kg, 57 kg, 166 kg and 500 kg, corresponding to charge groups 0.156 kg/m^3, 0.89 kg/m^3, 2.59 kg/m^3 and 7.81 kg/m^3, respectively.

The charge groups are far below the range of our experiments. Consequently, no direct comparison of the measured pressures, shown in table 6.3, and the pressures from the model tests can be done.

Eq (5.1) is fitted also to the Lista-pressures to compare the values of C_2 such obtained with the values of C_2 from the model tests. When $r_L = 0.06$ as the most probable value of wall roughness in the Lista tunnel, and the actual q-values from the Lista shots, are inserted in eq (5.11a) we can compare the attenuation in the Lista experiments with the attenuation found in the model tests.

The values of C_2 calculated from eq (5.11a) and from the Lista shots are shown in table 7.4. It should be noticed, however, that to use eq (5.11a) with these q-values is a considerable extrapolation from the q-values used to determine the parameters in the equation.

In spite of this, also the Lista experiments seem to support the conclusion that the attenuation of the front pressure decreases with increasing scale.

7.3.3 Summary

A comparison between model tests and geometrically and otherwise different full scale tests seems to give most information when the attenuation of the front pressure is examined.

C_2 seems to decrease also when the scale increases towards full scale. This is in accordance with the observations done in the small range of scales 1:100 - 3:100.

8 CONCLUSION

The primary objective of this work has been to examine the validity of scaling laws (eq 2.7 and 2.11) for explosions in underground installations. The results have shown that within the range of our small scales the deviation from scaling is highly significant. Further, it is clear that if the deviation from scaling with respect to dimension should continue to increase to the same degree outside our scaling range, then small scale testing would be quite unsuitable for predicting explosion effects in the full scale case.

This leads up to the secondary objective, to find possible corrections to the scaling laws, which make them suitable for such predictions. To achieve this it is necessary to identify the nonscaling effects. One possibility is that the main source for nonscaling is the attenuation of the blast wave due to small-scale roughness. An attempt to take this factor into account was presented in chapter 6. However, the time frame for the project did not allow an exhaustive analysis, so no firm conclusion has been reached.

It is believed, however, that the experimental data contained in this report, together with other available information, will make further progress possible. It is therefore recommended that sufficient resources should be allocated for a more detailed analysis. The purpose would then be prove if the hypothesis and correction method suggested in chapter 6 is correct, and to examine if simple considerations about energy and impulse of the blast wave can lead to useful conclusions.

References

(1) Rollvik, S
M Vigstad
- Investigation of underground explosions with model tests: Measurements on the platform, Intern rapport VM-61, NDRE (1978)

(2) Skarbøvik, K
M Vigstad
- Investigation of underground explosions with model tests: The experimental upset, Teknisk notat VM-309, NDRE (1978)

(3) Christoffersen, Ø
- Investigation of underground explosions with model tests: System description and some implementation details, Teknisk notat S-498, NDRE (1978)

(4) Schmidt, K G
- Investigation of underground explosions with model tests: Preliminary report II, Teknisk notat VM-238, NDRE (1976)

(5) Eriksson, S
- Fronttrykk och impuls hos endimensionell støtvåg vid detonation i tunnel. (Front pressure and impulse of an one-dimensional shock wave generated by a charge detonating in a tunnel) Report No 103:35, Royal Swedish Fortification Administration (1964)

(6) Skjeltorp, A T
A Jenssen
- One-dimensional blast wave propagation, Fourth International Symposium on the Military Applications of Blast Simulation (1974)

(7) Curran, D R
- Summary of experimental data regarding the pressures in underground tunnels resulting from underground explosions, Teknisk notat X-171, NDRE (1967)

(8) Dylewski, T J
- Criteria for selecting curves for fitting to data, AIAA Journal, vol 8, no 8 (1970)

(9) Curran, D R
- Underground storage of ammunition, experiments concerning accidental detonation in an underground chamber, Intern Rapport X-111, NDRE (1966)

(10) Hveding, D
- Shockwave- rough surface interaction, Teknisk notat F-315, NDRE (1977)

(11) Porzel, F B - Study of Shock impedance effects in a rough walled tunnel. Institute for Defence Analysis Research Paper P-330 (1969) (AD 684790)

(12) Bobin, L
Ch Thery - Ausbreitung und Dämpfung der Stosswellen in Stollen, Third International Symposium on the Military Applications of Blast Simulation (1972)

(13) Curran, D R - Effects of an explosion in an underground chamber, Teknisk notat X-132, NDRE (1965)

(14) Brode, H L
B R Parkin - Journal of Geophysical Res, 68, no 9, 2761-2789 (1963)

(15) - Operation Snowball Project Descriptions, Vol 1 (U) DASA 1516-1 (Project 1.2)

(16) Emrich, R J
C W Curtiss - J Appl Phys 24, 360 (1953)

(17) Schmidt, K G - Undergrond explosion trials at Raufoss 1968: Blast wave propagation following a detonation in a tunnel system, Intern rapport X-128, NDRE (1970)

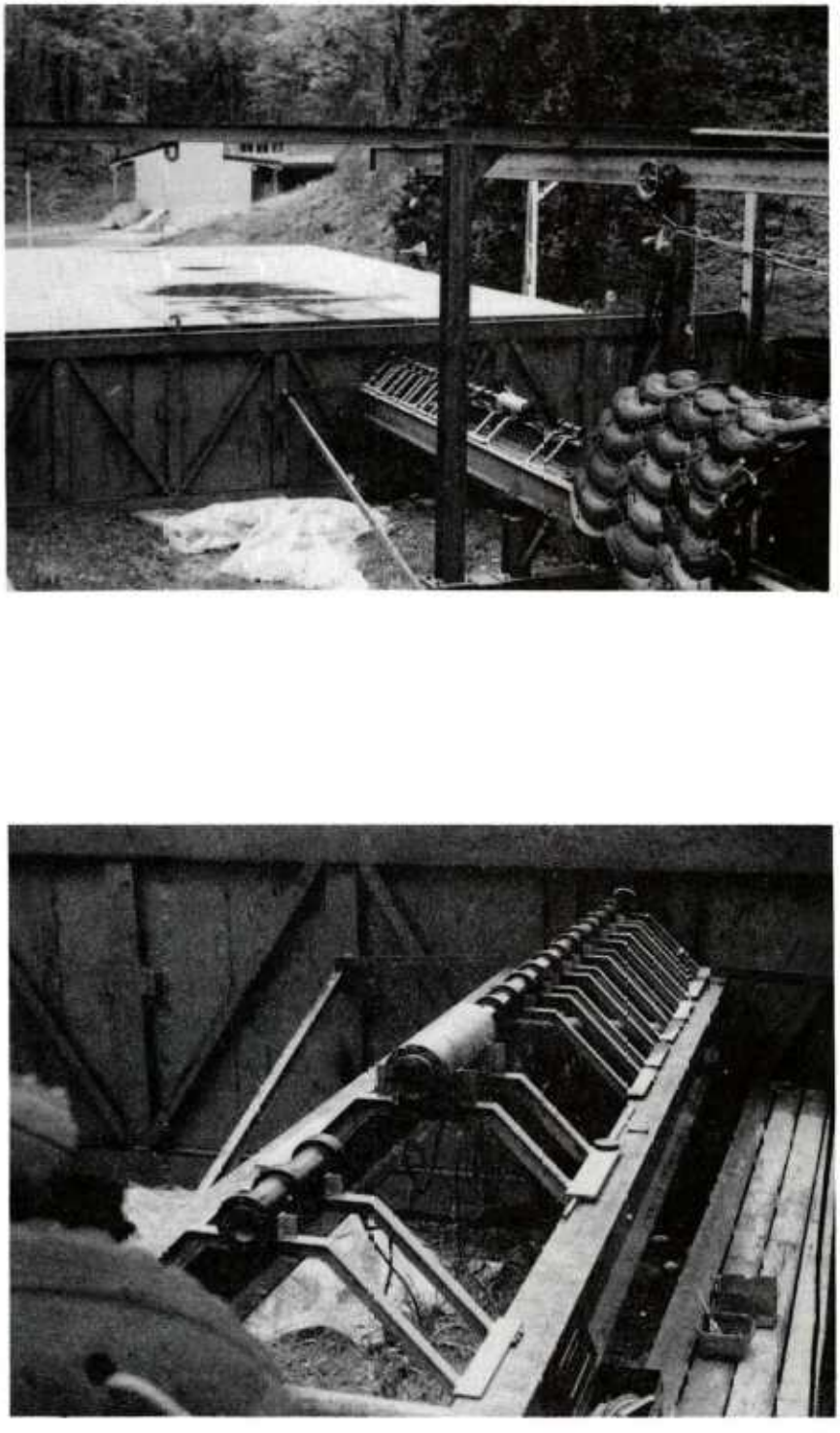

Figure 1 The experimental upset, scale 1:100

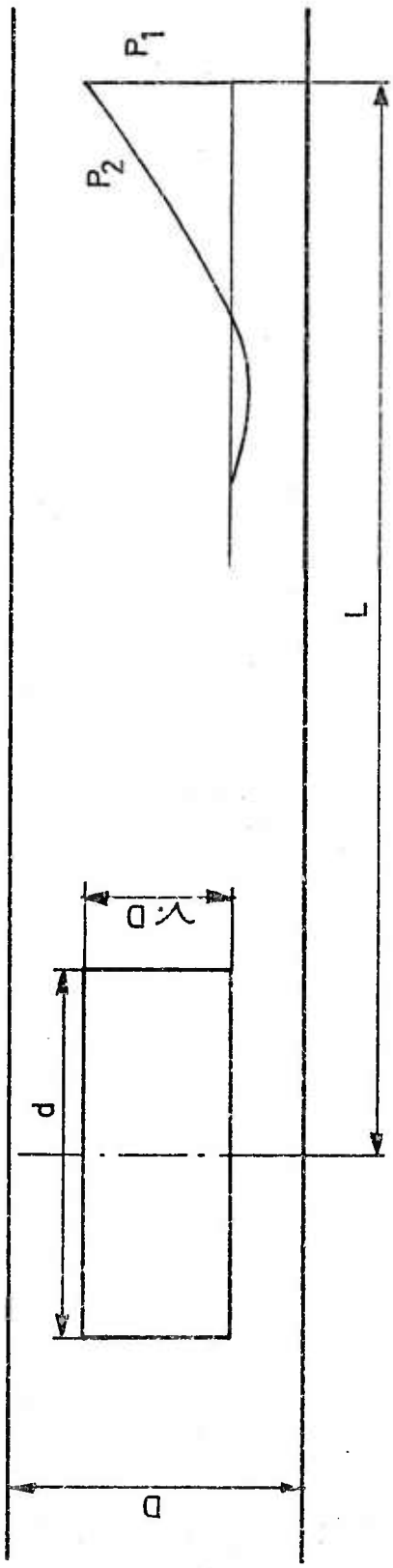

Figure 2.1 Sketch of tube with charge

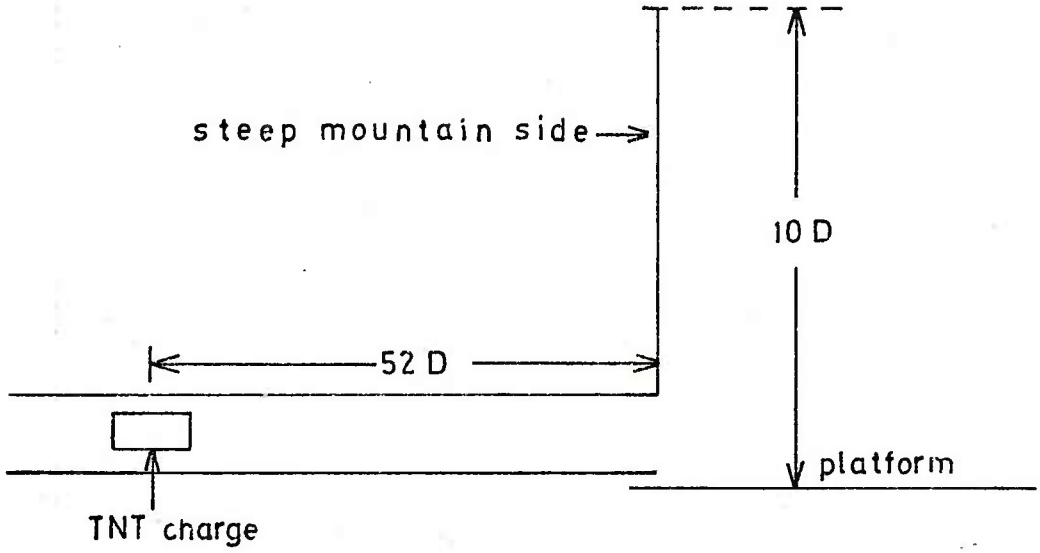

Figure 3.1 CFG 1 in principle

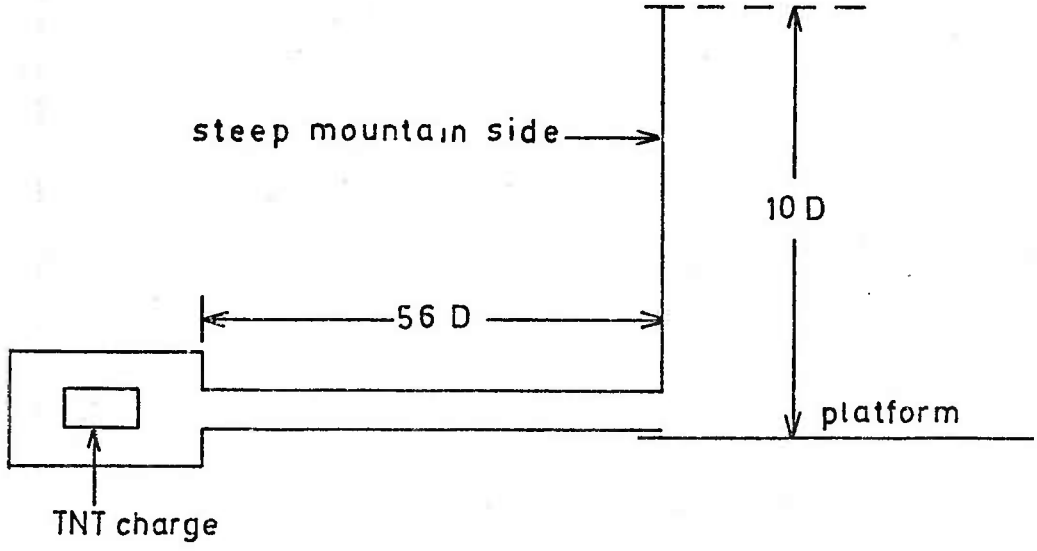

Figure 3.2 CFG 2 in principle

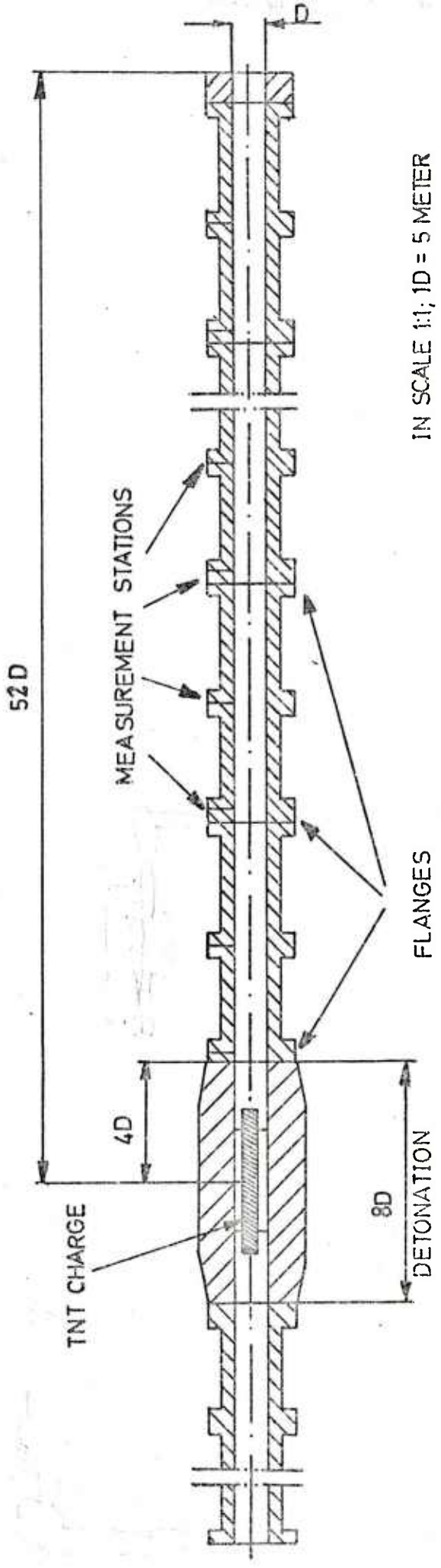

Figure 3.3 CFG 1

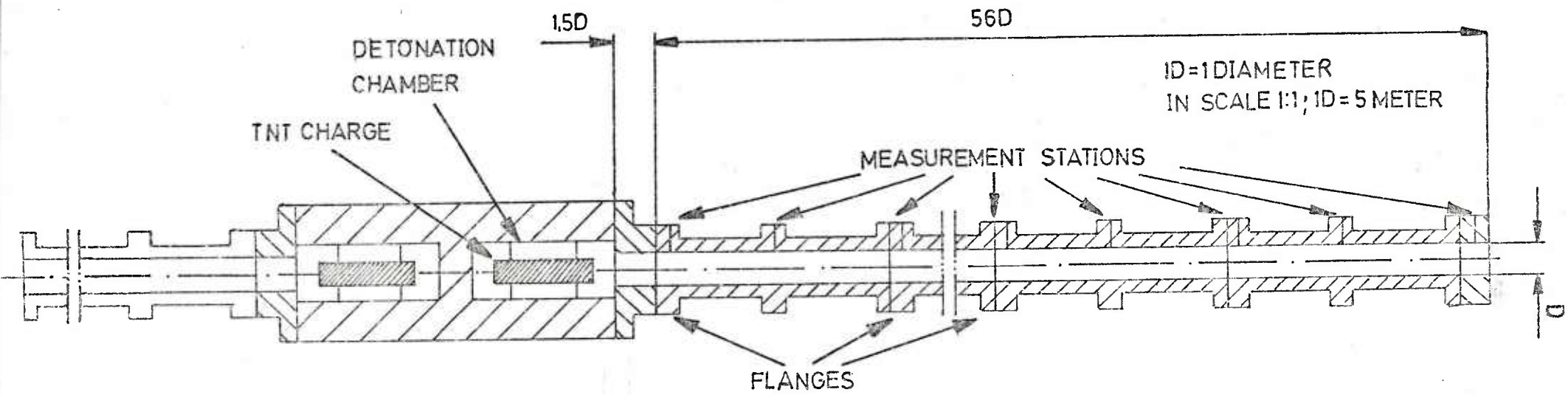

CROSS SECTION AREA TUBES : $A = \pi(D/2)^2$

CROSS SECTION AREA DETONATION CHAMBER : 2 A

Figure 3.4 CFG 2

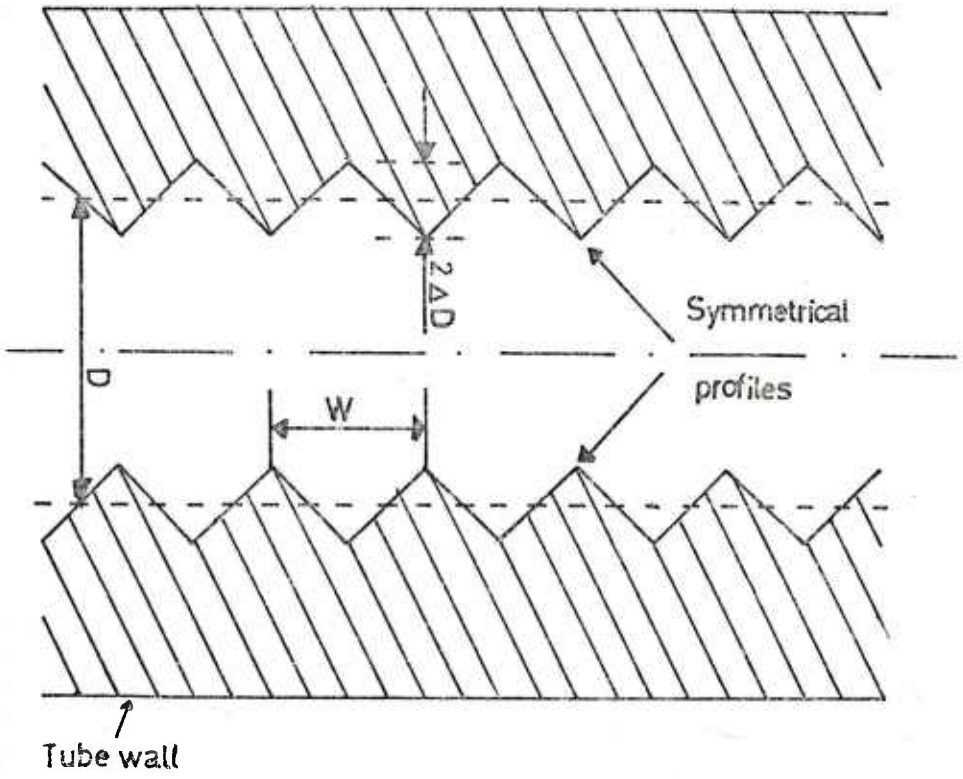

Definition of wall roughness: $r_t = \frac{\Delta D}{D}$

Scale	1/100	1/50	3/100
W(mm)	20	40	60

Figure 3.5 Definition of wall roughness

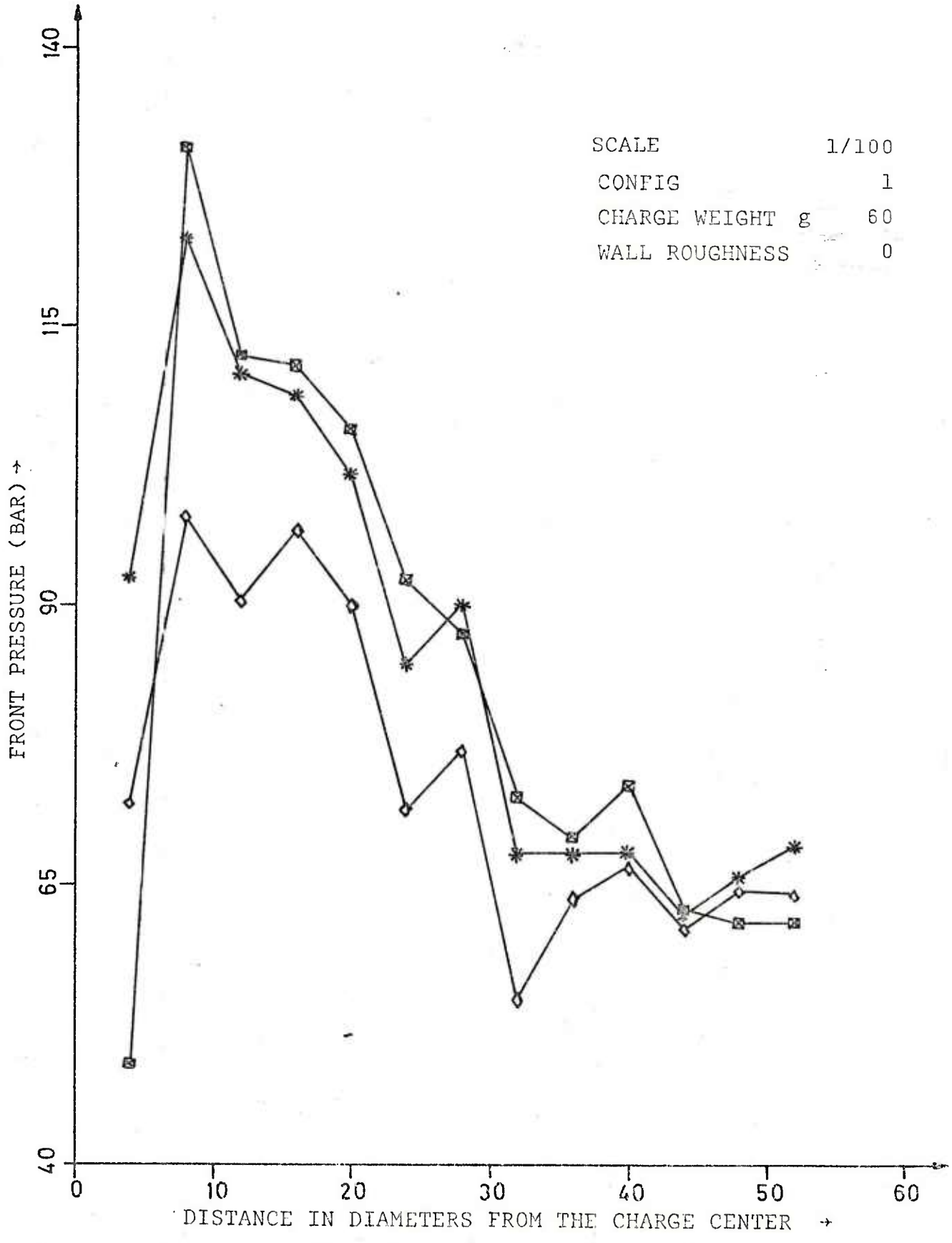

Figure 3.6 Front pressure versus distance

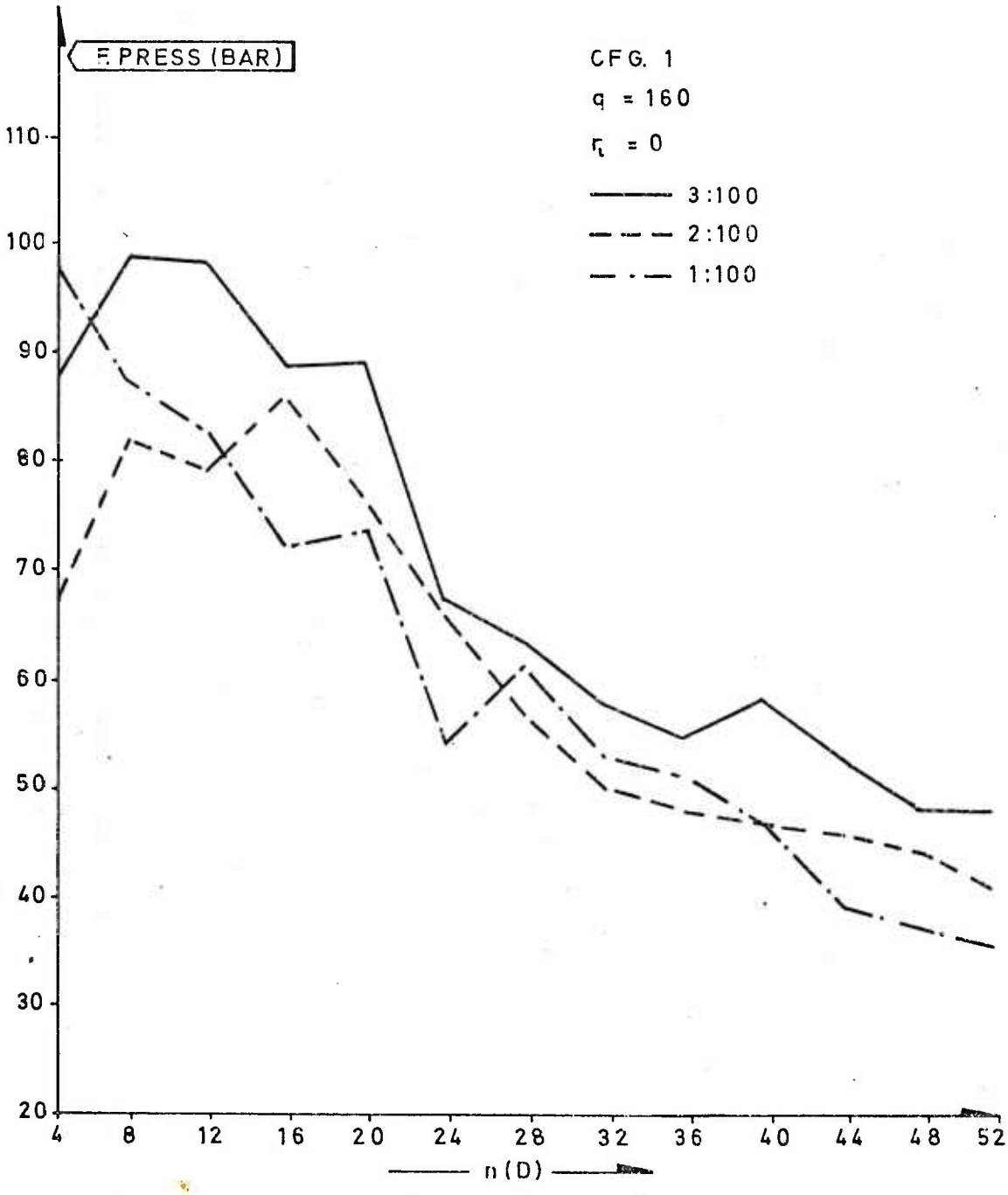

Figure 3.7 Mean values of front pressure versus distance in three scales

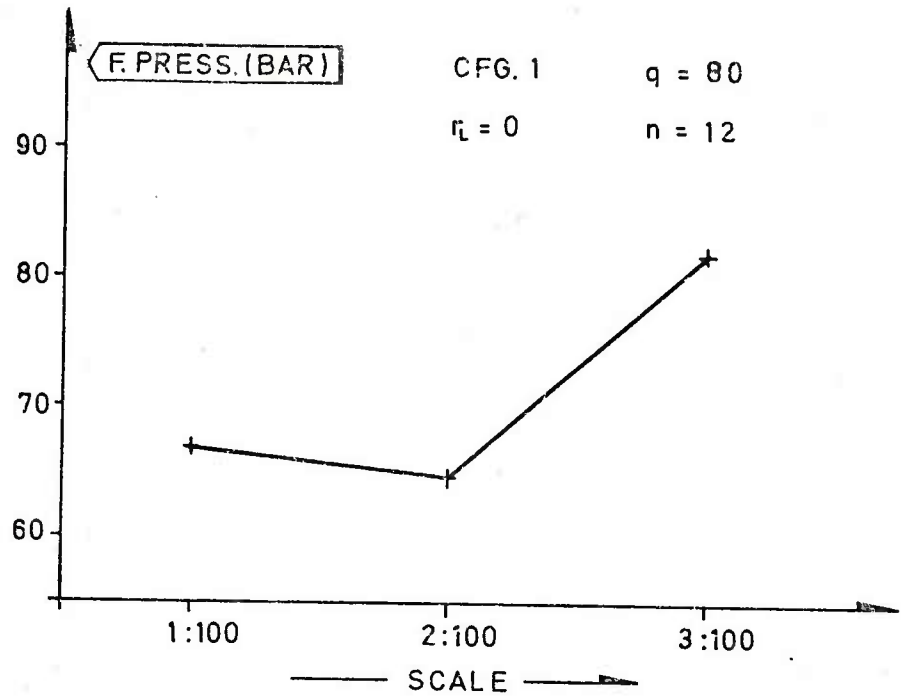

Figure 3.8a Deviation from scaling with respect to dimension

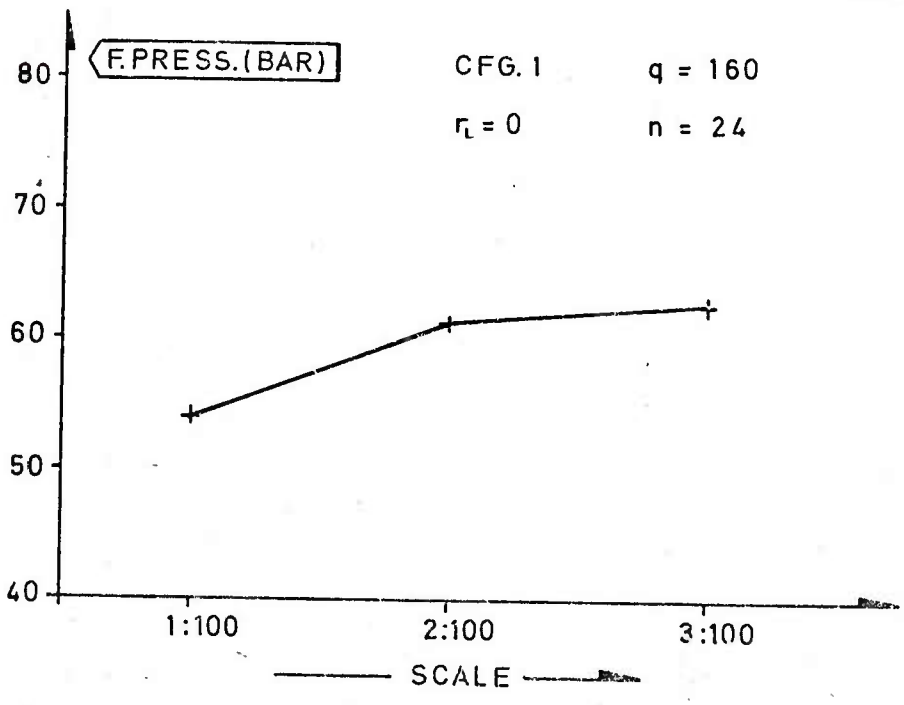

Figure 3.8b Deviation from scaling with respect to dimension

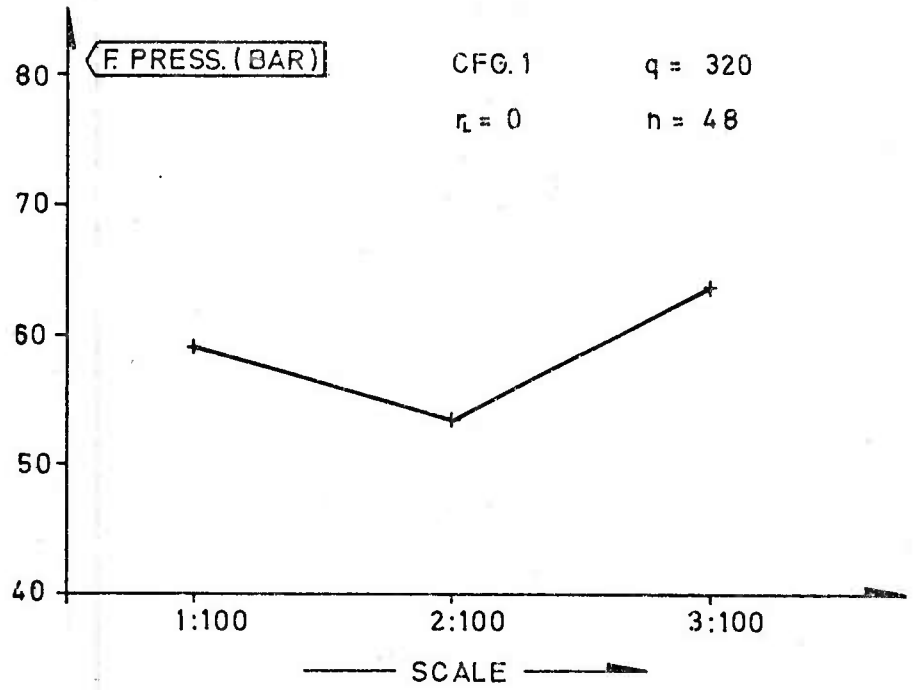

Figure 3.8c Deviation from scaling with respect to dimension

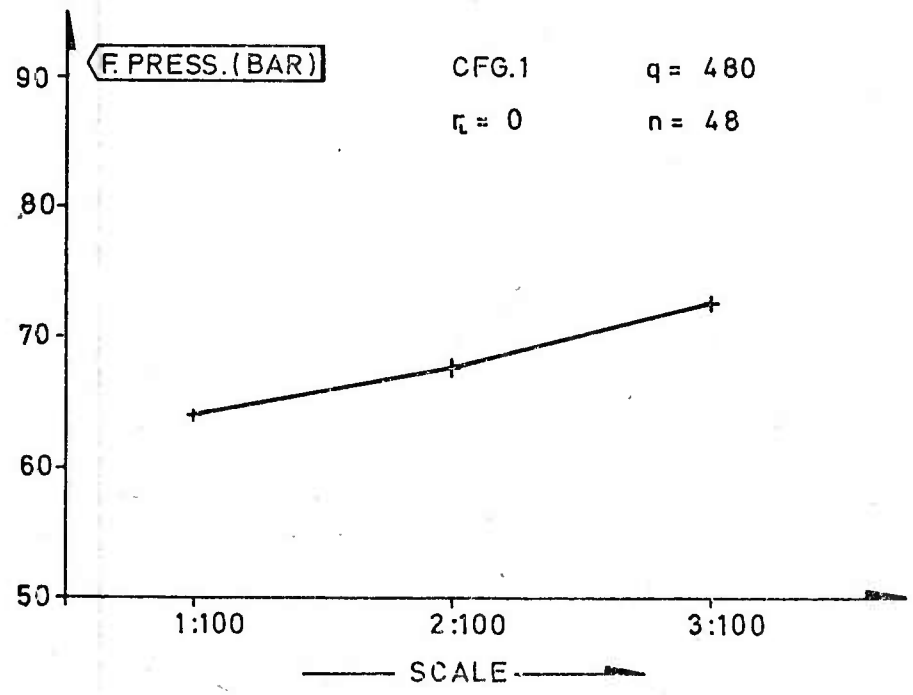

Figure 3.8d Deviation from scaling with respect to dimension

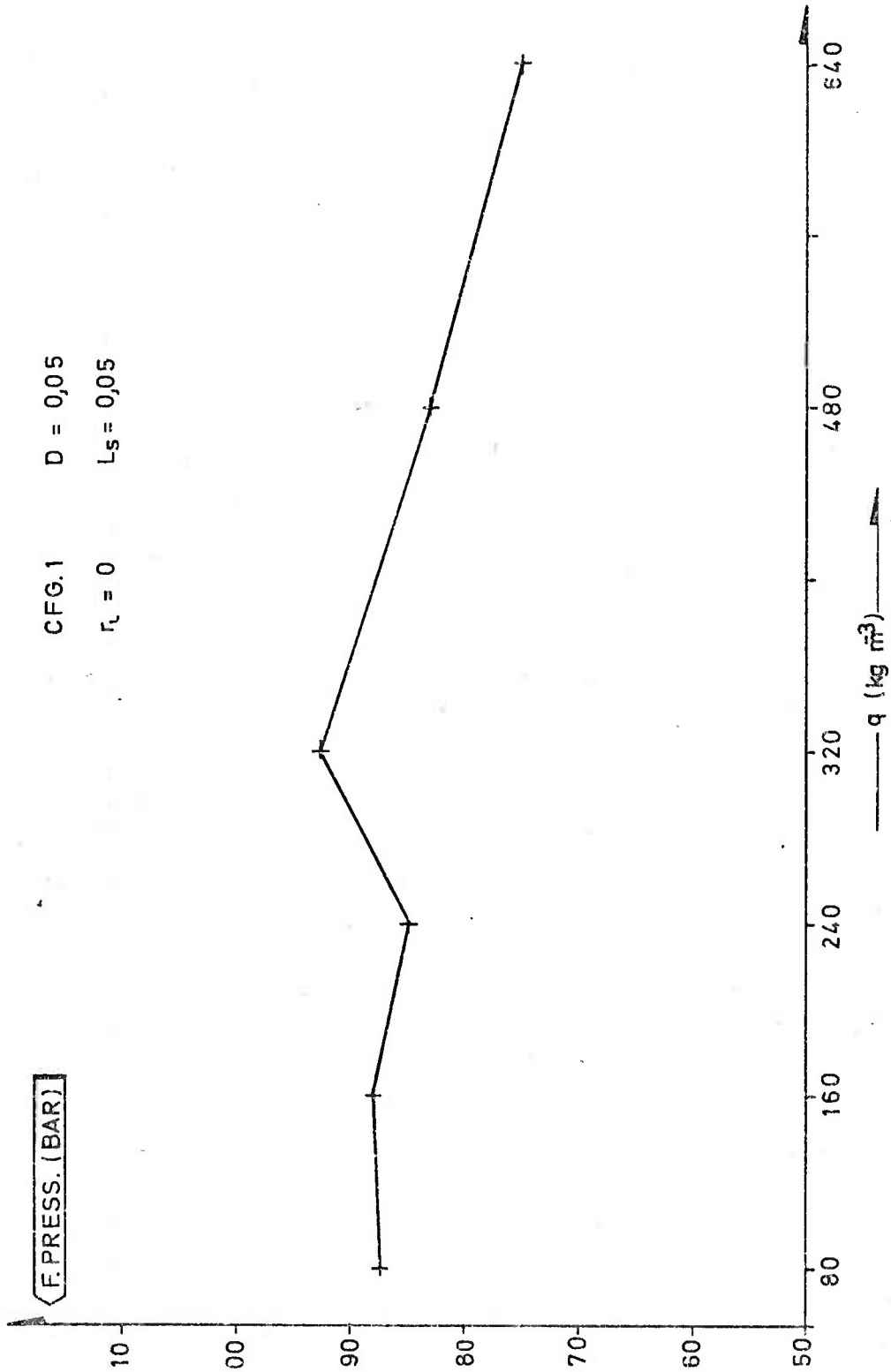

Figure 3.9a Deviation from self-similarity

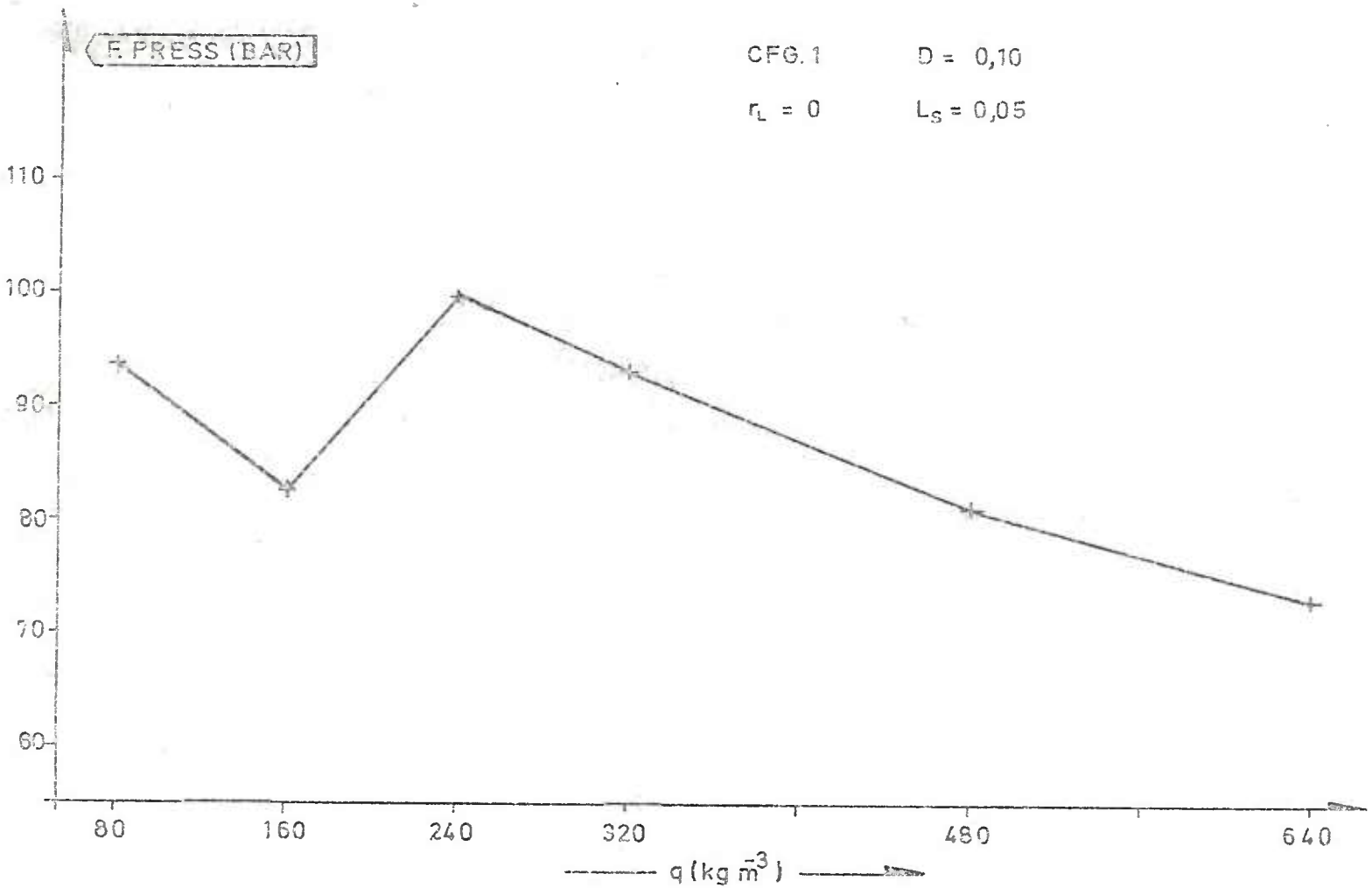

Figure 3.9b Deviation from self-similarity

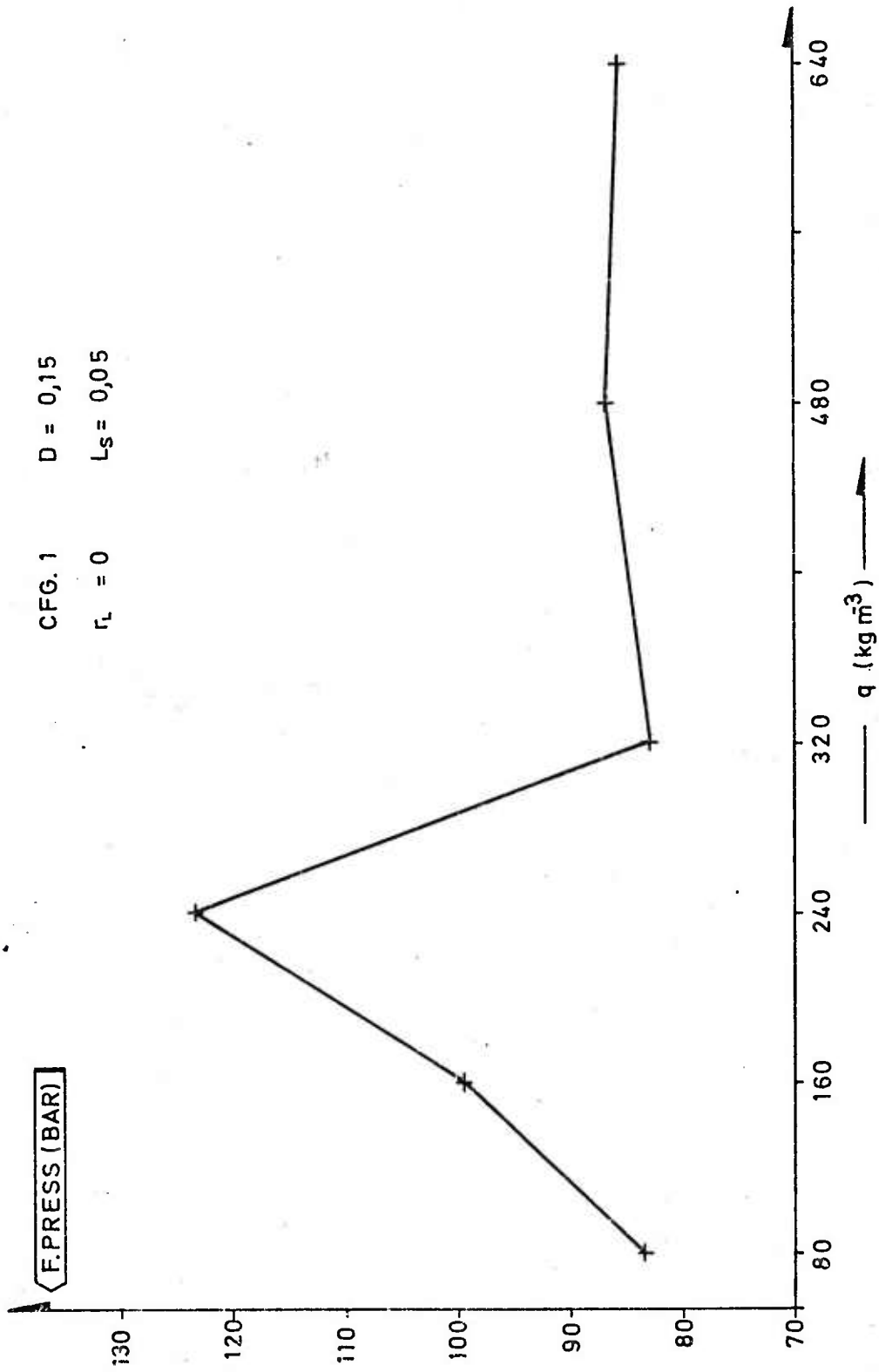

Figure 3.9c Deviation from self-similarity

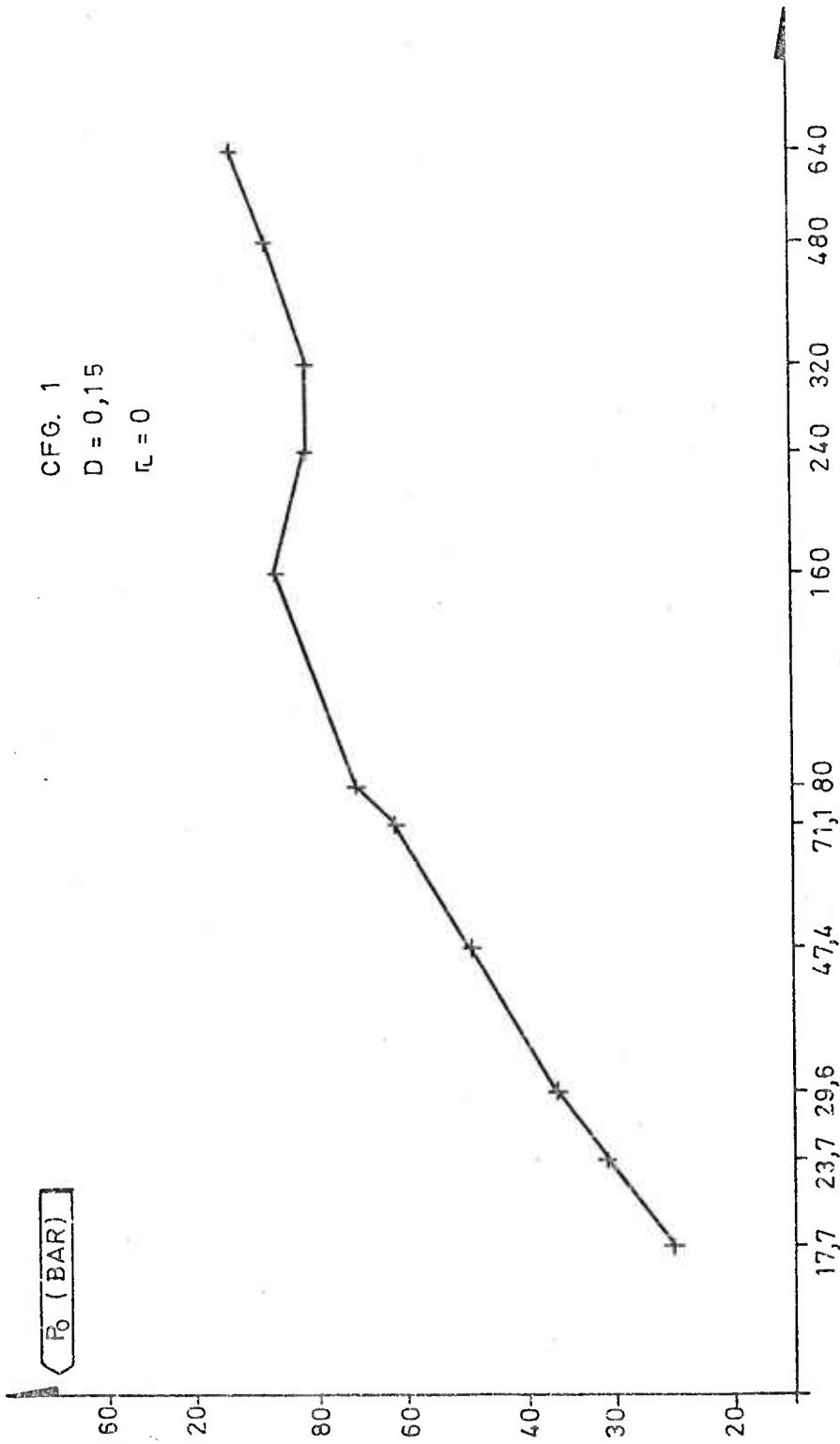

Figure 5.1a P_o from curve fitting as function of charge group. Logarithmic scale

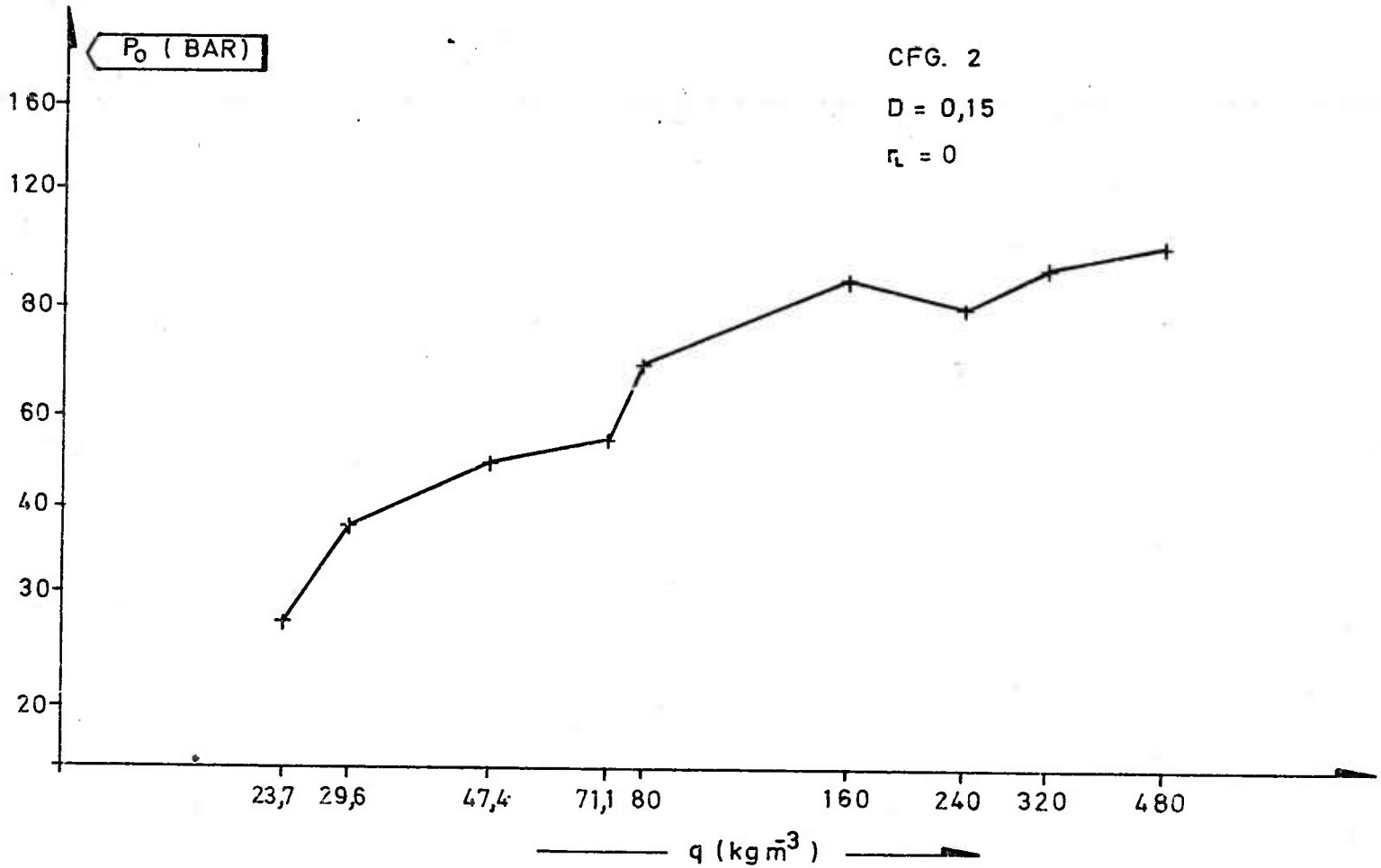

Figure 5.1b P_o from curve fitting as function of charge group. Logarithmic scale

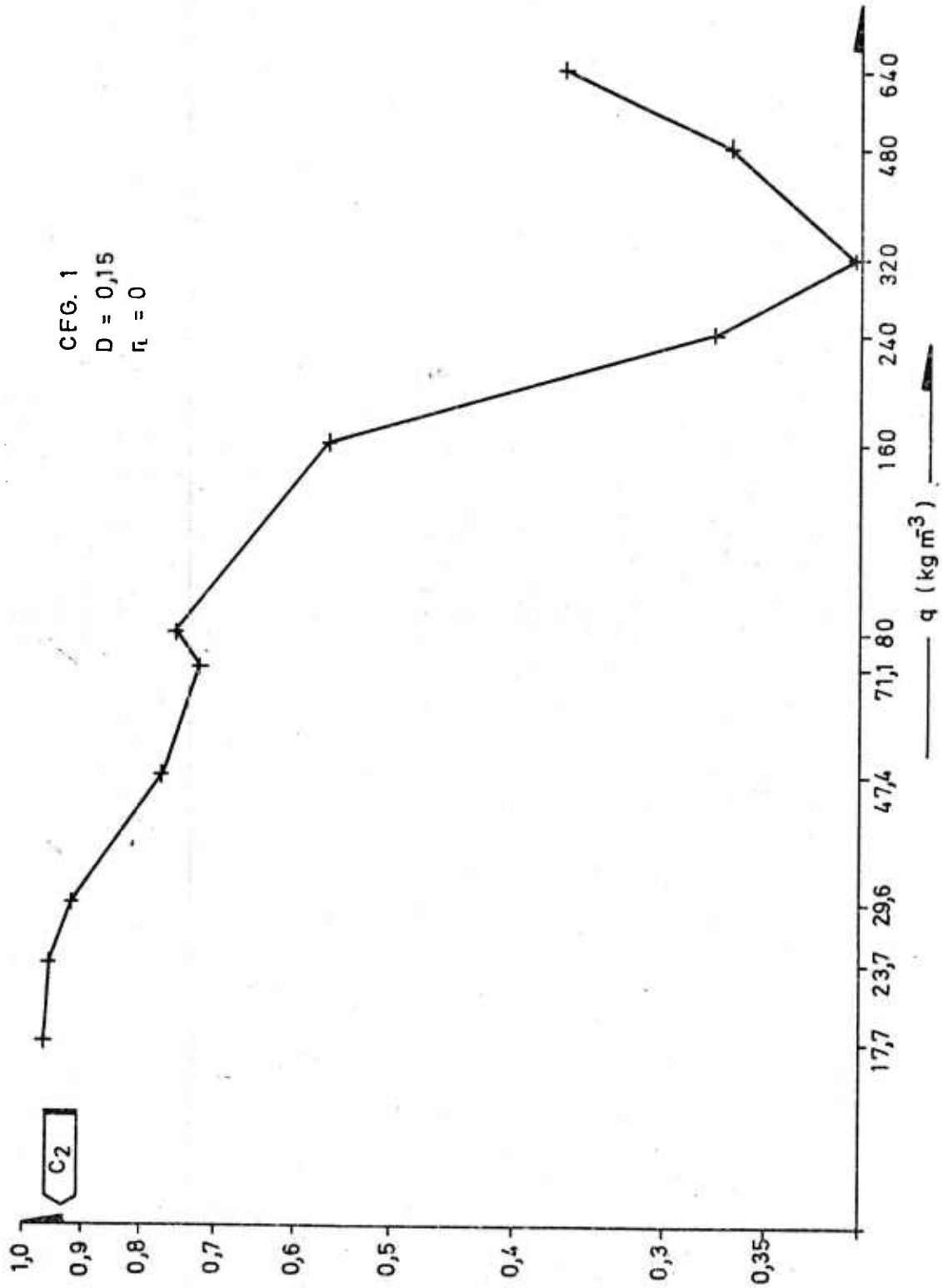

Figure 5.2a C_2 from curve fitting as function of charge group. Logarithmic scale

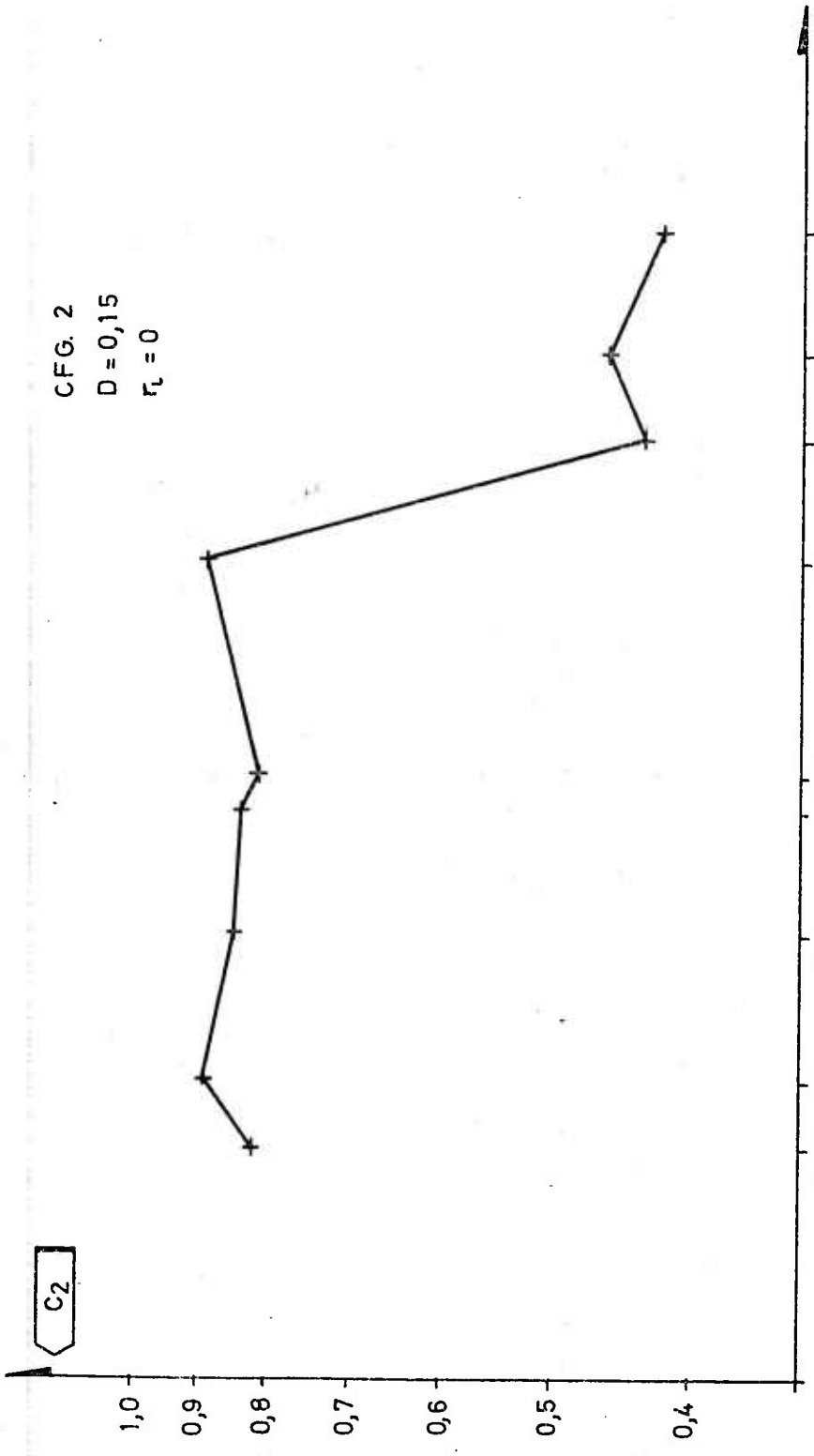

Figure 5.2b C_2 from curve fitting as function of charge group. Logarithmic scale

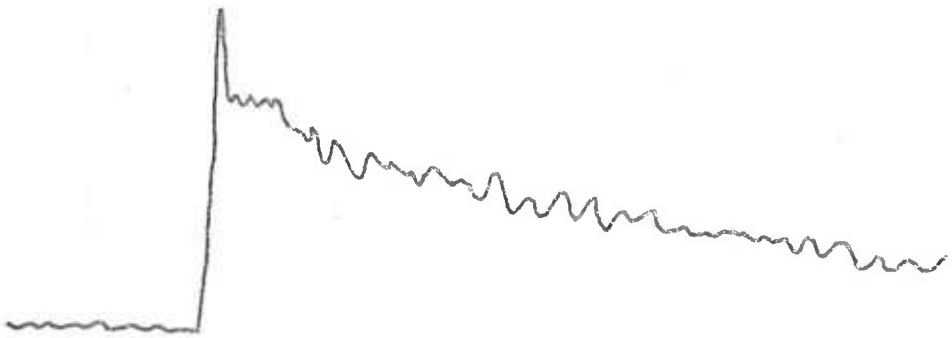

CFG 1

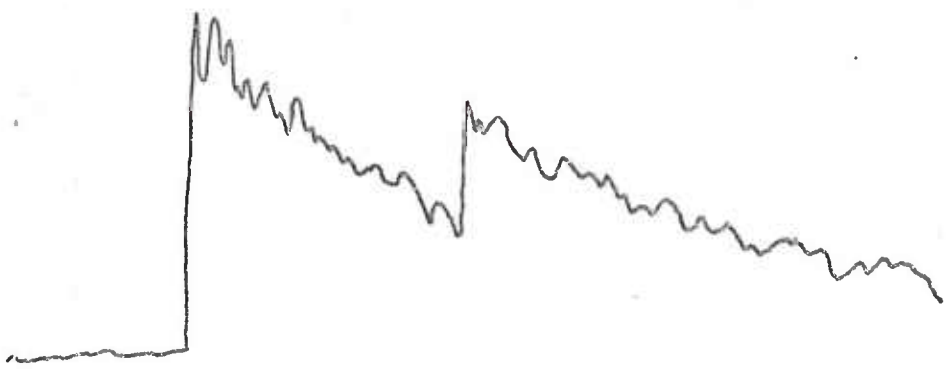

CFG 2

Figure 5.3 Difference in pressure-time profile between CFG 1 and CFG 2

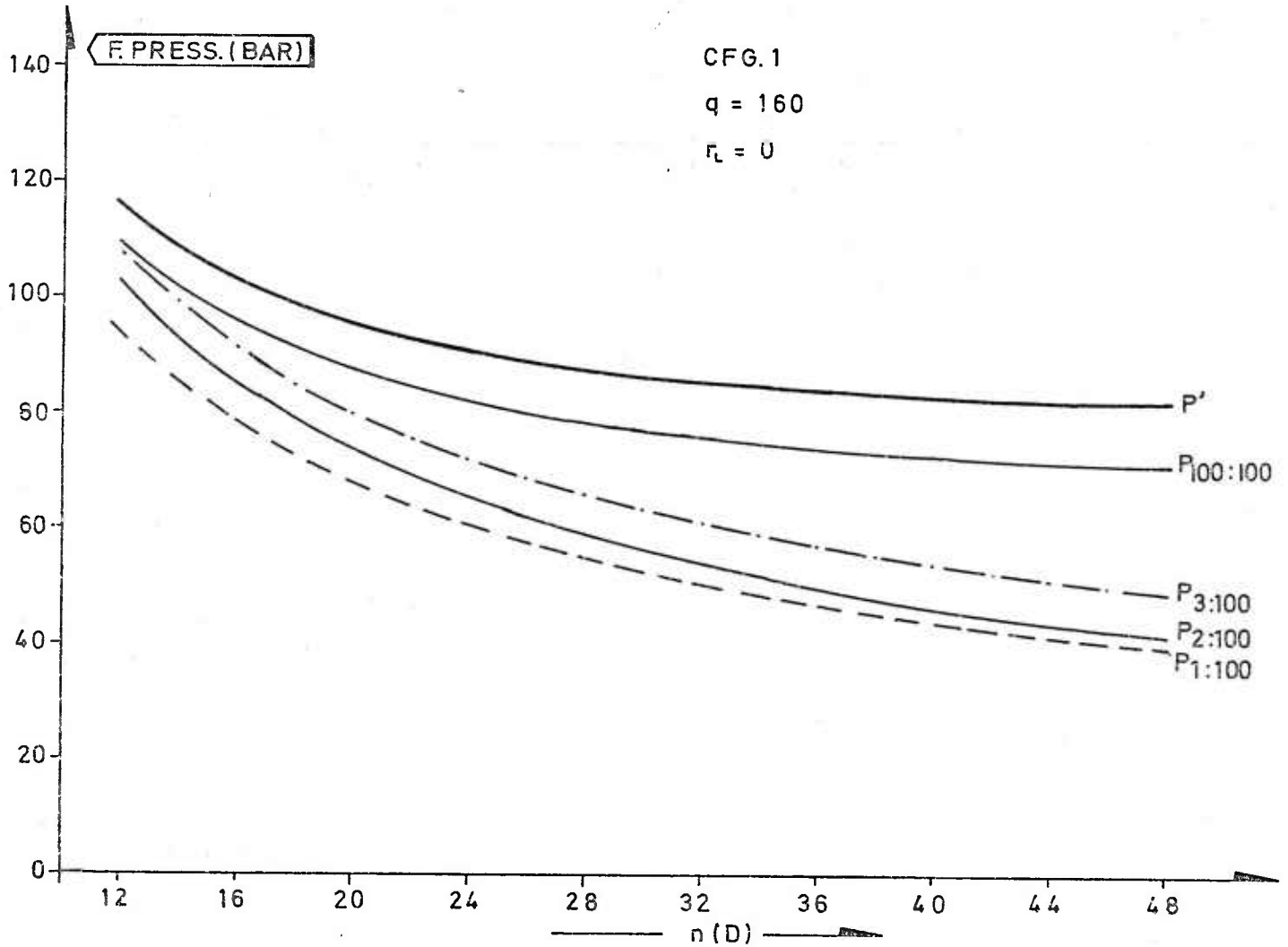

Figure 6.1 Front pressure in model tests, estimated front pressure in full scale and P' versus distance

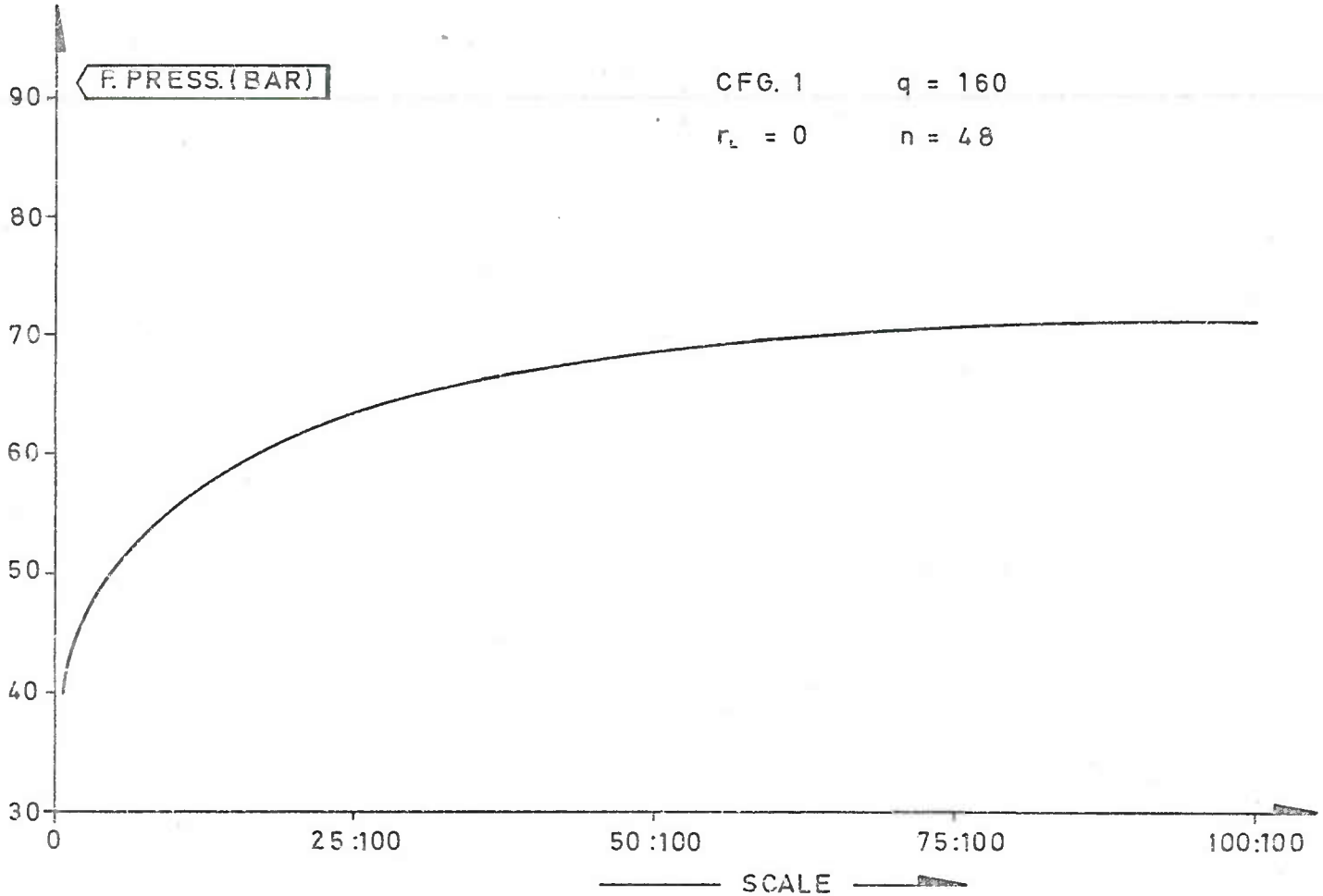

Figure 7.1 Attempt on extrapolation from small scales to large scales

	$q(kgm^{-3})$	80	160	240	320	480	640
Q (g TNT)	D=0.05m	10	20	30	40	60	80
	D=0.10m	80	160	240	320	480	640
	D=0.15m	270	540	810	1080	1620	2160
Q/V (kgm^{-3})	all D	12.5	25.0	37.5	50.0	75.0	100.0

Table 3.1 Charges in the main series of experiments

D = 0.15m	$q(kgm^{-3})$	17.8	23.7	29.6	47.4	71.1
Q (g TNT)	CFG 1	60	80	100	160	240
	CFG 2		80	100	160	240
Q/V kgm^{-3}		2.78	3.70	4.63	7.41	11.11

Table 3.2 Shots with small charges

ε	50%	20%	10%	5%	2%	1%	0.2%
C	0.674	1.282	1.645	1.960	2.326	2.576	3.090

Table 4.1 Test level and percentage points of Student's T-distribution

	CFG1			CFG 2		
r_L	0	0.03	0.06	0	0.03	0.06
α_1	164.4	160.2	218.0	218.0	97.0	165.4
T	5.106	3.046	3.417	6.687	2.526	3.725

Table 4.2a Values of α_1 and T in build-up region

	CFG1			CFG 2		
r_L	0	0.03	0.06	0	0.03	0.06
$\alpha_1' \times 10^4$	24.850	0.770	-4.405	-47.500	-69.500	-71.000
T	3.358	0.091	0.565	3.084	3.971	4.465

Table 4.2b Values of α_1' and T in build-up region

	CFG1			CFG 2		
r_L	0	0.03	0.06	0	0.03	0.06
α_1	32.8	18.1	71.4	64.2	32.6	50.0
T	4.530	3.591	15.000	9.093	6.342	12.755

Table 4.3a Values of α_1 and T in attenuation region

	CFG1			CFG 2		
r_L	0	0.03	0.06	0	0.03	0.06
$\alpha_1' \times 10^3$	0.655	-2.650	-7.400	-9.600	-15.650	-15.650
T	0.712	1.456	2.966	5.647	3.525	4.369

Table 4.3b Values of α_1' and T in attenuation region

	CFG 1			CFG 2		
r_L	0	0.03	0.06	0	0.03	0.06
$\alpha_2 \times 10^2$	-2.688	-2.400	-1.338	-2.788	-5.588	-4.900
T	3.258	3.975	2.352	2.411	6.507	7.582
$\alpha_3 \times 10^1$	-1.080	-4.530	-7.850	-2.600	-1.670	-4.420
T	1.306	7.342	13.534	2.031	1.740	6.173

Table 4.4a Values of α_2, α_3 and corresponding T-values in attenuation region

	CFG 1			CFG 2		
r_L	0	0.03	0.06	0	0.03	0.06
$\alpha_2' \times 10^6$	-2.063	-23.094	-49.375	-10.594	-29.750	-50.313
T	1.654	9.146	14.234	3.498	3.437	7.630
$\alpha_3' \times 10^4$	1.243	5.525	10.325	2.725	7.050	11.075
T	7.565	16.617	22.692	6.566	6.104	12.621

Table 4.4b Values of α_2', α_3' and corresponding T-values in attenuation region

$q = 80\ kgm^{-3}$		CFG 1				CFG 2			
D(m)	r_L	C_1	C_2	P_o(bar)	R	C_1	C_2	P_o(bar)	R
0.05	0	21.22	0.61	56.4	0.91	15.13	0.77	52.4	0.94
	0.03	6.67	1.26	51.1	0.96	6.29	1.05	33.9	0.96
	0.06	2.69	1.65	38.4	0.96	3.64	1.23	26.5	0.97
0.10	0	18.91	0.75	63.2	0.96	17.07	0.68	50.8	0.95
	0.03	6.06	1.18	40.5	0.96	5.13	1.09	29.7	0.83
	0.06	4.71	1.36	42.3	0.96	3.59	1.33	30.3	0.90
0.15	0	21.07	0.75	70.1	0.97	17.91	0.81	66.3	0.95
	0.03	10.86	0.86	43.5	0.96	7.25	1.08	41.1	0.95
	0.06	4.28	1.51	48.6	0.98	4.94	1.15	31.6	0.97

Table 5.1a Results from curve fitting, $q = 80\ kg/m^3$

$q = 160 kgm^{-3}$		CFG 1				CFG 2			
D(m)	r_L	C_1	C_2	P_o(bar)	R	C_1	C_2	P_o(bar)	R
0.05	0	18.34	0.63	78.0	0.77	16.24	0.60	65.0	0.91
	0.03	5.24	1.07	60.9	0.96	3.51	1.13	47.4	0.97
	0.06	1.77	1.51	56.9	0.96	2.23	1.23	38.2	0.98
0.10	0	19.03	0.65	84.7	0.96	16.99	0.58	64.6	0.89
	0.03	8.97	0.78	53.5	0.94	4.73	1.00	46.7	0.94
	0.06	2.25	1.44	62.4	0.97	3.28	1.09	40.6	0.90
0.15	0	24.60	0.57	90.7	0.94	11.41	0.89	88.0	0.89
	0.03	6.26	0.97	58.4	0.97	6.00	0.96	55.3	0.97
	0.06	2.39	1.42	62.2	0.97	2.64	1.29	51.5	0.98

Table 5.1b Results from curve fitting, $q = 160\ kg/m^3$

$q = 240 kgm^{-3}$		CFG 1				CFG 2			
D(m)	r_L	C_1	C_2	P_o(bar)	R	C_1	C_2	P_o(bar)	R
0.05	0	26.93	0.44	88.1	0.87	20.38	0.49	77.7	0.93
	0.03	5.54	0.93	69.3	0.93	3.82	1.00	57.1	0.96
	0.06	0.81	1.56	55.0	0.89	1.05	1.38	44.6	0.93
0.10	0	29.72	0.36	78.5	0.90	19.16	0.50	74.7	0.91
	0.03	5.12	0.93	63.1	0.94	3.47	1.01	53.2	0.89
	0.06	0.93	1.59	69.6	0.87	1.94	1.21	51.4	0.95
0.15	0	38.98	0.27	82.0	0.77	24.88	0.43	79.7	0.95
	0.03	6.25	0.88	68.3	0.95	5.02	0.93	62.0	0.95
	0.06	2.42	1.23	67.5	0.93	1.83	1.26	55.8	0.96

Table 5.1c Results from curve fitting, q = 240 kg/m^3

$q = 320 kgm^{-3}$		CFG 1				CFG 2			
D(m)	r_L	C_1	C_2	P_o(bar)	R	C_1	C_2	P_o(bar)	R
0.05	0	26.53	0.42	92.5	0.87	22.69	0.44	84.8	0.94
	0.03	7.05	0.75	67.4	0.92	4.54	0.85	58.2	0.94
	0.06	0.97	1.38	60.6	0.91	0.94	1.36	55.0	0.97
0.10	0	28.51	0.35	81.0	0.65	23.22	0.41	78.3	0.88
	0.03	6.14	0.75	57.7	0.86	3.67	0.90	54.5	0.90
	0.06	2.05	1.17	67.1	0.90	1.97	1.11	55.9	0.97
0.15	0	43.45	0.21	82.1	0.75	23.29	0.46	91.8	0.95
	0.03	8.32	0.69	65.3	0.96	4.40	0.89	63.7	0.94
	0.06	2.59	1.10	70.4	0.91	1.84	1.15	57.1	0.95

Table 5.1d Results from curve fitting, q = 320 kg/m^3

$q = 480 kgm^{-3}$		CFG 1				CFG 2			
D(m)	r_L	C_1	C_2	P_o(bar)	R	C_1	C_2	P_o(bar)	R
0.05	0	18.79	0.51	105.2	0.88	23.38	0.39	88.2	0.78
	0.03	5.58	0.73	67.7	0.93	3.21	0.90	69.6	0.95
	0.06	1.57	1.08	61.6	0.90	1.12	1.16	57.4	0.97
0.10	0	26.22	0.38	94.1	0.91	21.65	0.39	81.9	0.93
	0.03	4.68	0.78	67.5	0.85	3.67	0.90	78.6	0.96
	0.06	2.40	0.98	67.0	0.95	1.70	1.03	56.5	0.96
0.15	0	37.83	0.27	93.9	0.87	24.01	0.42	99.2	0.90
	0.03	7.63	0.67	75.1	0.96	4.28	0.80	65.2	0.88
	0.06	3.80	0.85	74.3	0.90	1.53	1.10	64.7	0.94

Table 5.1e Results from curve fitting, q = 480 kg/m^3

$q = 640 kgm^{-3}$		CFG 1				CFG 2			
D(m)	r_L	C_1	C_2	P_o(bar)	R	C_1	C_2	P_o(bar)	R
0.05	0	15.54	0.54	115.7	0.94	22.61	0.37	89.3	0.70
	0.03	4.73	0.75	75.0	0.96	3.41	0.80	65.6	0.79
	0.06	1.17	1.12	71.5	0.96	1.13	1.06	56.5	0.91
0.10	0	25.44	0.35	92.5	0.90				
	0.03	5.23	0.72	74.9	0.97				
	0.06	1.82	0.98	67.6	0.94				
0.15	0	27.28	0.36	104.7	0.87				
	0.03	8.84	0.57	71.1	0.91				
	0.06	4.12	0.76	69.1	0.90				

Table 5.1f Results from curve fitting, q = 640 kg/m^3

CFG 1 $P_o = aq^b$

D(m)	r_L	a	b	R	P_o(q=80)
0.05	0	13.8	0.33	0.99	59.0
	0.03	25.9	0.17	0.93	53.3
	0.06	13.5	0.26	0.93	41.7
0.10	0	31.8	0.17	0.89	66.9
	0.03	12.9	0.27	0.96	42.5
	0.06	20.0	0.20	0.81	48.7
0.15	0	36.8	0.15	0.84	72.3
	0.03	16.4	0.24	0.92	47.2
	0.06	23.8	0.18	0.89	52.4

Table 5.2a Dependence of P_o on q

CFG 2 $P_o = aq^b$

D(m)	r_L	a	b	R	P_o(q=80)
0.05	0	16.8	0.27	0.97	54.6
	0.03	8.5	0.33	0.96	36.4
	0.06	5.3	0.39	0.96	28.5
0.10	0	13.8	0.30	0.98	51.6
	0.03	3.4	0.50	0.98	30.5
	0.06	6.1	0.37	0.97	31.5
0.15	0	28.2	0.20	0.90	68.8
	0.03	13.8	0.26	0.95	43.6
	0.06	6.6	0.38	0.94	34.8

Table 5.2b Dependence of P_o on q

$C_2 = a + bD$

CFG 1	$r_L = 0$			$r_L = 0.03$			$r_L = 0.06$		
$q(kgm^{-3})$	a	b	R	a	b	R	a	b	R
80	0.56	1.4	0.87	1.50	-4.0	0.94	1.65	-1.4	0.48
160	0.68	-0.6	0.72	1.04	-1.0	0.35	1.55	-0.9	0.95
240	0.53	-1.7	1.00	0.96	-0.5	0.87	1.79	-3.3	0.82
320	0.54	-2.1	0.98	0.79	-0.6	0.87	1.50	-2.8	0.96
480	0.63	-2.4	1.00	0.79	-0.6	0.55	1.20	-2.3	0.99
640	0.60	-1.8	0.84	0.86	-1.8	0.93	1.31	-3.6	0.99

Table 5.3a Dependence of C_2 on D

$C_2 = a + bD$

CFG 2	$r_L = 0$			$r_L = 0.03$			$r_L = 0.06$		
$q(kgm^{-3})$	a	b	R	a	b	R	a	b	R
80	0.71	0.4	0.30	1.04	0.3	0.72	1.32	-0.8	0.45
160	0.40	2.9	0.84	1.20	-1.7	0.95	1.14	0.6	0.30
240	0.53	-0.6	0.79	1.05	-0.7	0.80	1.40	-1.2	0.69
320	0.42	0.2	0.40	0.84	0.4	0.75	1.42	-2.1	0.78
480	0.37	0.3	0.87	0.97	-1.0	0.87	1.16	-0.6	0.46

Table 5.3b Dependence of C_2 on D

$b = b_1 q + b_2$						
	CFG 1			CFG 2		
r_L	$b_1 \cdot 10^3$	b_2	R	$b_1 \cdot 10^3$	b_2	R
0	-4.9	0.36	0.72	-2.7	1.34	0.32
0.03	2.2	-2.13	0.35	-0.8	-0.33	0.14
0.06	-3.6	-1.24	0.70	-1.8	-0.37	0.28

Table 5.4 a and b Interaction between charge group and scale

$C_2 = aq^b$

		CFG 1			CFG 2		
D(m)	r_L	a	b	R	a	b	R
0.05	0	0.91	-0.10	0.46	3.76	-0.37	0.99
	0.03	4.35	-0.28	0.95	2.13	-0.15	0.84
	0.06	4.40	-0.21	0.89	1.67	-0.06	0.42
0.10	0	4.15	-0.40	0.87	1.38	-0.18	0.62
	0.03	2.60	-0.21	0.82	1.78	-0.11	0.93
	0.06	3.73	-0.20	0.74	2.19	-0.12	0.82
0.15	0	5.05	-0.47	0.73	6.39	-0.45	0.84
	0.03	2.60	-0.22	0.82	2.16	-0.16	0.98
	0.06	7.70	-0.35	0.95	1.41	-0.03	0.33

Table 5.5 a and b Dependence of C_2 on q

$$C_2 = a + br_L$$

CFG 1	D = 0.05 m			D = 0.10 m			D = 0.15 m		
$q(kgm^{-3})$	a	b	R	a	b	R	a	b	R
80	0.65	17.3	0.99	0.79	10.2	0.97	0.66	12.7	0.93
160	0.63	14.7	1.00	0.56	13.2	0.93	0.56	14.2	1.00
240	0.42	18.7	0.99	0.35	20.5	1.00	0.31	16.0	0.99
320	0.37	16.0	0.98	0.35	13.7	1.00	0.22	14.8	1.00
480	0.49	9.5	0.99	0.41	10.0	0.98	0.31	9.7	0.97
640	0.51	9.7	0.99	0.37	10.5	0.99	0.36	6.7	1.00

Table 5.6a Dependence of C_2 on r_L

$$C_2 = a + br_L$$

CFG 2	D = 0.05			D = 0.10			D = 0.15		
$q(kgm^{-3})$	a	b	R	a	b	R	a	b	R
80	0.79	7.7	0.99	0.71	10.8	0.99	0.84	5.7	0.95
160	0.67	10.5	0.93	0.64	8.5	0.94	0.84	6.7	0.94
240	0.51	14.8	0.99	0.55	11.8	0.97	0.46	13.8	0.99
320	0.42	15.3	1.00	0.46	11.7	0.97	0.49	11.5	0.99
480	0.43	12.8	0.98	0.45	10.7	0.94	0.43	11.3	1.00
640	0.40	11.5	0.99						

Table 5.6b Dependence of C_2 on r_L

CFG 1

i =	1	2	3	4	5	6	7
β_i	1.09	2.0	27.6	-0.094	-20	-0.55	-2.2
R_i		0.32	0.90	0.21	0.26	0.15	0.34

Table 5.7a Results from linear regression on C2

CFG 2

i =	1	2	3	4	5	6	7
β_i	1.47	2.75	-6.16	-0.175	-24	-0.42	2.7
R_i		0.23	0.23	0.18	0.16	0.05	0.19

Table 5.7b Results from linear regression on C_2

CFG 1 r_L = 0							
D(m)	curve	q=80	q=160	q=240	q=320	q=480	q=640
0.05	I	2.17	1.44	1.25	1.53	1.20	1.02
	II	3.04	1.09	1.02	2.62	2.41	2.01
0.10	I	1.61	2.81	1.46	2.41	7.14	1.50
	II	2.83	78.56	2.80	2.23	4.50	1.73
0.15	I	1.25	1.12	1.08	2.09	1.99	3.82
	II	1.10	2.02	1.06	1.95	3.74	2.19

Table 5.8 Comparison between curveforms

D = 0.15 r_L = 0						
CFG	Q(g)	q(kgm^{-3})	C_1	C_2	P_o(bar)	R
1	60	17.8	22.54	0.96	24.9	0.99
	80	23.7	21.29	0.95	31.0	0.99
	100	29.6	20.68	0.92	36.4	0.98
	160	47.4	20.87	0.77	48.1	0.98
	240	71.1	21.00	0.72	61.4	0.98
2	80	23.7	19.59	0.82	27.0	0.75
	100	29.6	21.90	0.89	37.9	0.94
	160	47.4	18.91	0.84	47.2	0.98
	240	71.1	14.70	0.83	51.0	0.95

Table 5.9 Results from curve fitting
Shots with small charges

$q(kgm^{-3})$	n: / D(m)	4	8	12	16	20	24	28	32	36	40	44	48
80	0.05	3333	3077	2395	2139	2312	2073	1932	2000	1747	1786	2030	1739
	0.10	3620	2930	2581	2417	2292	2162	2073	1946	1878	1835	1758	1691
	0.15	3448	2857	2597	2410	2277	2174	2058	1993	1905	1849	1794	1714
160	0.05	3738	3077	2740	2597	2597	2667	2410	2614	2667	2105	1961	2168
	0.10	4233	3101	2797	2667	2685	2564	2417	2319	2279	2241	2122	2046
	0.15	3822	3085	2797	2626	2691	2685	2490	2395	2312	2210	2131	2069
240	0.05	3738	3252	3252	2721	2857	2500	2312	2614	2500	2454	2299	2260
	0.10	4545	3604	2963	2817	2667	2581	2589	2516	2462	2417	2319	2254
	0.15	4225	3343	3030	2721	2715	2752	2559	2542	2495	2424	2344	2277
320	0.05	4444	3333	3150	3077	3008	2721	2454	2548	2548	2410	2395	2439
	0.10	4734	3653	3053	2817	2730	2548	2454	2417	2477	2548	2402	2247
	0.15	4396	3550	3191	2934	2824	2709	2564	2603	2626	2581	2516	2449
480	0.05	5000	3333	3077	3150	3008	3008	2857	2548	2667	2614	2439	2548
	0.10	5031	4624	3292	3150	2963	2847	2768	2614	2548	2524	2524	2548
	0.15	4598	3582	3324	3061	2934	2857	2679	2609	2564	2581	2609	2521
640	0.05	5195	3636	3540	3175	3540	3279	2395	2469	2920	2667	2797	2857
	0.10	4969	3922	3306	3113	2930	2768	2685	2581	2532	2477	2432	2469
	0.15	4743	3715	3438	3117	2978	2927	2791	2721	2649	2586	2526	2490

Table 6.1 Shock velocities (ms^{-1})

CFG 1 $r_L = 0$		P'(2:100)/P'(1:100) = I P'(3:100)/P'(2:100) = II								
$q(kgm^{-3})$	n:	16	20	24	28	32	36	40	44	48
80	I	1.11	1.05	1.06	1.05	1.04	1.03	1.02	1.01	1.00
	II	1.06	1.07	1.04	1.03	1.02	1.01	1.01	1.00	1.00
160	I	1.09	1.08	1.07	1.07	1.05	1.04	1.04	1.04	1.03
	II	1.02	1.03	1.04	1.04	1.04	1.04	1.03	1.03	1.03
240	I	0.94	0.95	0.96	0.98	0.99	0.99	1.00	1.00	1.01
	II	1.00	1.01	1.02	1.02	1.02	1.02	1.02	1.03	1.03
320	I	0.91	0.92	0.92	0.93	0.94	0.94	0.95	0.96	0.96
	II	0.98	1.00	1.02	1.03	1.04	1.05	1.05	1.06	1.07
480	I	0.95	0.98	0.99	1.01	1.02	1.03	1.03	1.04	1.09
	II	0.93	0.94	0.95	0.96	0.96	0.97	0.97	0.97	0.97
640	I	0.83	0.85	0.87	0.89	0.91	0.92	0.92	0.93	0.93
	II	1.07	1.06	1.05	1.05	1.04	1.04	1.04	1.03	1.02

Table 6.2 Values of $\frac{P'(2:100)}{P'(1:100)}$ and $\frac{P'(3:100)}{P'(2:100)}$

SHOT 2	Q = 100 kg		q = 5.4 kgm^{-3}	
n	7.1	10.9	14.7	18.4
P(bar)	12.6	8.4	5.4	5.2

SHOT 6	Q = 300 kg		q = 16.1 kgm^{-3}			
n	7.1	10.9	14.7	18.4	26.1	29.9
P(bar	26.4	15.9	12.7	7.1	6.7	2.7

SHOT 8	Q = 1000 kg		q = 53.7 kgm^{-3}			
n	8.3	12.0	15.8	19.6	27.3	31.0
P(bar)	59.5	40.7	19.0	15.7	13.7	6.0

SHOT 9	Q = 1000 kg		q = 53.7 kgm^{-3}		
n	6.7	14.2	18.0	25.7	29.5
P(bar)	85.9	20.7	18.5	12.5	4.4

Table 7.1a Results from Raufoss experiments

CFG 1	D = 0.15		r_L = 0		
n \ q (kgm^{-3})	17.8	23.7	29.6	47.4	71.1
4	78.8	86.0	93.7	108.8	113.1
8	47.6	58.4	63.3	79.1	82.3
12	29.1	37.3	42.0	53.2	64.6
16	25.6	30.1	35.6	46.5	59.7
20	19.7	25.3	29.3	39.8	51.2
24	16.0	20.9	25.4	34.6	45.5
28	15.2	18.8	22.5	33.3	43.6
32	12.9	16.5	20.2	29.8	39.8

Table 7.1b Some results from model tests, small charges

CFG 1		q = 80 kgm^{-3}			q = 160 kgm^{-3}		
r	D (m) / r_L	0.05	0.10	0.15	0.05	0.10	0.15
4	0	87.4	95.5	83.4	98.6	67.2	88.2
	0.03	90.1	62.3	82.1	83.7	37.3	77.7
	0.06	42.5	53.7	80.7	75.6	64.4	97.8
8	0	74.0	71.4	77.3	87.9	82.3	99.3
	0.03	68.0	47.6	72.2	81.7	66.1	79.9
	0.06	45.3	46.9	60.9	67.6	58.1	72.6
12	0	66.6	64.3	81.8	83.1	79.6	98.7
	0.03	50.9	40.3	56.5	61.1	51.3	63.9
	0.06	46.6	35.9	49.2	60.8	44.5	53.7
16	0	53.7	61.4	63.0	72.4	86.3	89.2
	0.03	48.7	34.6	39.9	55.6	50.1	57.3
	0.06	32.7	38.0	45.3	45.5	55.9	53.8
20	0	49.9	55.3	64.6	74.0	76.8	89.5
	0.03	38.1	31.9	34.8	48.3	44.5	45.0
	0.06	30.9	33.6	32.1	43.3	42.7	42.7
24	0	46.5	48.4	53.0	54.0	66.4	67.7
	0.03	33.2	28.0	34.4	39.7	38.8	38.0
	0.06	18.1	27.6	29.7	36.0	39.8	40.9
28	0	39.9	44.2	50.2	61.5	56.9	64.1
	0.03	38.2	23.0	28.2	37.8	34.3	36.5
	0.06	17.3	20.1	23.2	29.4	30.7	31.0
32	0	36.3	37.3	39.8	53.1	50.2	58.0
	0.03	19.8	20.2	24.4	30.3	36.9	32.5
	0.06	12.5	16.6	18.4	20.7	24.5	26.3

Table 7.1c Some results from model tests, main series

D (m) / q (kgm^{-3})	0.05	0.10	0.15	2.65 (Raufoss)
5.4	2.19	2.17	2.14	1.00
16.1	1.90	1.85	1.79	1.40
53.7	1.60	1.51	1.42	1.75 (1.57)

Table 7.2 Values of C_2 obtained from the Raufoss experiments and from the model tests

Q = 10 kg	q = 0.16 kgm^{-3}			
n	2.25	5.00	8.75	14.50
P (bar)	1.9	1.4	1.0	0.4

Q = 57 kg	q = 0.89 kgm^{-3}				
n	2.0	5.0	10.0	14.5	20.0
P (bar)	6.3	3.7	2.0	1.8	1.3

Q = 166 kg	q = 2.6 kgm^{-3}			
n	5.0	7.5	12.5	22.5
P (bar)	9.3	7.5	4.0	2.3

Q = 500 kg	q = 7.8 kgm^{-3}					
n	3.5	5.0	6.5	10.0	20.0	27.5
P (bar)	34.0	21.0	13.6	6.9	3.8	2.6

Table 7.3 Results from Lista experiments

D(m) / q(kgm^{-3})	0.05	0.10	0.15	4.0 (Lista)
0.16	3.26	3.35	3.44	0.78
0.89	2.81	2.86	2.90	0.68
2.6	2.54	2.56	2.57	0.97
7.8	2.26	2.25	2.23	1.24

Table 7.4 Values of C_2 obtained from the Lista experiments and the model tests